

TRANSMISSION ELECTRON MICROSCOPY
CHARACTERIZATION OF
LONG WAVELENGTH DILUTE NITRIDES

A DISSERTATION

SUBMITTED TO THE DEPARTMENT OF MATERIALS SCIENCE AND
ENGINEERING

AND THE COMMITTEE ON GRADUATE STUDIES

OF STANFORD UNIVERSITY

IN PARTIAL FULFILLMENT OF THE REQUIREMENTS

FOR THE DEGREE OF

DOCTOR OF PHILOSOPHY

Tihomir Gugov

April 2005

© Copyright by Tihomir Gugov 2005

All Rights Reserved

I certify that I have read this dissertation and that in my opinion it is fully adequate, in scope and quality, as dissertation for the degree of Doctor of Philosophy.

James Harris (Principal Advisor)

I certify that I have read this dissertation and that in my opinion it is fully adequate, in scope and quality, as dissertation for the degree of Doctor of Philosophy.

William Nix

I certify that I have read this dissertation and that in my opinion it is fully adequate, in scope and quality, as dissertation for the degree of Doctor of Philosophy.

Ann Marshall

Approved for the University Committee on Graduate Studies

Abstract

The quaternary GaInNAs alloy is a very promising material system for optical sources in the 1.2-1.6 μm range with application in telecommunication fiber-optic networks. Unfortunately, this is not a thermodynamically stable alloy and considerable growth challenges need to be overcome to improve the optical emission efficiency of the material. Considerable progress in dealing with these difficulties has been made for alloys containing around 30% indium and 2% nitrogen which emit light around 1.3 μm . The effort to push emission out to 1.5 μm , the wavelength for long-haul networks, by adding more indium (up to 40%) has proven considerably more difficult. Recently, the addition of small amounts of antimony has put this alloy back on track for the 1.5 μm challenge by dramatically improving the luminescence efficiency of the material.

In this work, several different Transmission Electron Microscopy (TEM) techniques are used for the first time as powerful tools in the structural characterization of GaInNAs(Sb) quantum well structures at the atomic level. High Resolution TEM (HRTEM) is used to map out the local strain and compositional fluctuations in the quantum wells and barriers. This is correlated with Energy-Filtered TEM (EFTEM) imaging, Dark-Field (DF) imaging with the (002) and (220) reflections, and Energy Dispersive X-ray Spectroscopy (EDX) profiles across the quantum well regions. Both GaInNAs and GaInNAsSb samples were characterized with these techniques. We found that indium tends

to segregate in GaInNAs samples while the antimony is responsible for more uniform distribution of indium in the GaInNAsSb samples.

The results of this work bring further understanding of the performance of real devices. GaInNAs lasers are known to have broad emission spectra and high threshold currents. Researchers have speculated that this could be due to local compositional fluctuations. Our results confirm that these indeed occur and give considerable insight into the role of antimony in improving the material quality and luminescence efficiency.

Acknowledgements

First and foremost, I would like to thank my advisor on this work, Professor James Harris (a.k.a. the Coach). Thanks Coach for all the mentorship, precious advice and great conversations during my PhD years! It has been a great experience.

Further, I would like to thank the faculties of the Materials Science Department and the Electrical Engineering Department for their wonderful teaching and research support. I especially want to thank the members of my Orals Committee Mark Cappelli, Bill Nix, Ann Marshall and Paul McIntyre and the members of my Reading Committee Bill Nix and Ann Marshall.

I am really grateful to Gail Chun-Creech and Stephanie Sorensen for always being available and helpful with administrative issues.

Next, I want to thank all the MBE growers for their help, collaboration and wonderful GaInNAs material: Mark, Vincent, Homan, Seth, Wonill, Soo and Hopil.

I want to thank the present and former Harris group members for their friendship and support: Vince Lordi, Xiaojun, Junxian, Kai, David, Xian, Chang, Lynford, Rafael, Vijit, Glenn, Dan, Gigi, Ke, Evan, Rekha, Ali.

I also want to thank Christian Kisielowski, Cheng Yu Song and Alfredo Tolley at NCEM at LBNL for all their help with the TEM analysis.

I especially want to thank Kerstin Volz for her TEM mentorship and precious advice.

This work was possible through the generous support of the Stanford Graduate Fellowship and the DARPA/ONR Optoelectronics Materials Center.

Finally, I want to thank the people who have the biggest contribution in getting me to this stage: my mother and my father. Thank you!

Table of Contents

Abstract.....	iv
Acknowledgements.....	vi
List of Figures.....	ix
Chapter 1: Introduction.....	1
1.1 Requirements for Modern Fiber-Optic Networks.....	1
1.2 Material Choices for Long-Wavelength Emission.....	6
1.3 Role of TEM in Understanding and Improving the Material.....	13
Chapter 2: TEM Techniques.....	16
2.1 Cross-Section TEM Sample Preparation.....	16
2.2 High Resolution Imaging (HRTEM).....	20
2.3 Energy-Filtered TEM (EFTEM).....	38
2.4 Energy Dispersive X-ray Spectroscopy (EDX).....	41
2.5 Dark-Field (DF) Imaging.....	44
Chapter 3: Effect of Growth Conditions on the Microstructure.....	54
3.1 Growth Temperature Effects.....	54
3.2 Anneal Effects.....	61
3.3 Deflection Plates Effects.....	65
Chapter 4: Conclusions and Future Work.....	72
4.1 Conclusions.....	72
4.2 Future Work.....	73
Chapter 5: References.....	75

List of Figures

Figure 1.1: Schematic of a typical fiber-optic telecommunications network.....	2
Figure 1.2: Dependence of fiber loss on transmission wavelength in the silica fiber.....	3
Figure 1.3: Dependence of the transmission distance on the transmission speed.....	5
Figure 1.4: Bandgap dependence on the lattice parameter for some important III-V alloys.....	7
Figure 1.5: Schematic of a VCSEL structure.....	10
Figure 2.1: Configuration for cross-section TEM sample with the electron beam along the [110] zone axis.....	18
Figure 2.2: High Resolution (HRTEM) imaging configuration.....	21
Figure 2.3: HRTEM image of the quantum well area of a GaInNAs sample.....	22
Figure 2.4: Selection of the original HRTEM image.....	24
Figure 2.5: Filtered image.....	25
Figure 2.6: Filtered image with fitted peaks.....	26
Figure 2.7: Filtered image with fitted lattice.....	27
Figure 2.8: Strain map across a single quantum well GaInNAs sample.....	28
Figure 2.9: Strain map of a triple quantum well GaInNAs(Sb) sample.....	31
Figure 2.10: Extended strain map along the bottom well of GaInNAs(Sb).....	32
Figure 2.11: Extended strain map along the middle well of GaInNAs(Sb).....	33
Figure 2.12: Extended strain map along the top well of GaInNAs(Sb).....	33

Figure 2.13: Photoluminescence spectra of GaInNAs and GaInNAs(Sb) samples.....	35
Figure 2.14: Cathodoluminescence spectra of GaInAs, GaInNAs and GaInNAs(Sb) samples.....	36
Figure 2.15: Indium EFTEM map of triple quantum well GaInNAs(Sb) sample.....	39
Figure 2.16: Intensity profile across the EFTEM image in Fig. 2.15.....	40
Figure 2.17: EDX spectrum across triple quantum well GaInNAs(Sb).....	42
Figure 2.18: Image of sample area where the probe was scanned.....	42
Figure 2.19: EDX spectrum across single quantum well GaInNAs.....	43
Figure 2.20: Image of sample area where the probe was scanned.....	43
Figure 2.21: Dark-field imaging configuration.....	45
Figure 2.22: [110] zone axis diffraction pattern.....	46
Figure 2.23: DF (004) image of a single quantum well GaInNAs sample.....	48
Figure 2.24: Schematic of the (002) imaging condition.....	49
Figure 2.25: Schematic of the (004) imaging condition.....	49
Figure 2.26: DF (002) image of triple quantum well GaInNAs sample.....	51
Figure 2.27: DF (002) image of triple quantum well GaInNAs(Sb) sample.....	52
Figure 3.1: Strain map of triple quantum well GaInNAs(Sb) sample. The temperature was constant during growth.....	55
Figure 3.2: Strain map of triple quantum well GaInNAs(Sb) sample. The temperature was dropped 5 °C per quantum well.....	56

Figure 3.3: DF (002) image of triple quantum well GaInNAs(Sb) sample. The temperature was constant during growth.....	58
Figure 3.4: DF (002) image of triple quantum well GaInNAs(Sb) sample. The temperature was dropped 5 °C per quantum well.....	59
Figure 3.5: DF (220) image of triple quantum well GaInNAs(Sb) sample. The temperature was constant during growth.....	60
Figure 3.6: DF (220) image of triple quantum well GaInNAs(Sb) sample. The temperature was dropped 5 °C per quantum well.....	61
Figure 3.7: Strain map of unannealed triple quantum well GaInNAs(Sb) sample.....	63
Figure 3.8: Strain map of annealed triple quantum well GaInNAs(Sb) sample.....	64
Figure 3.9: Strain map of a single quantum well GaInNAs(Sb) sample. No deflection plates.....	66
Figure 3.10: Strain map of a single quantum well GaInNAs(Sb) sample. With deflection plates.....	67
Figure 3.11: DF (002) image of a single quantum well GaInNAs(Sb) sample. No deflection plates.....	68
Figure 3.12: DF (002) image of a single quantum well GaInNAs(Sb) sample. With deflection plates.....	69
Figure 3.13: DF (220) image of a single quantum well GaInNAs(Sb) sample. No deflection plates.....	70

Figure 3.14: DF (220) image of a single quantum well GaInNAs(Sb)

sample. With deflection plates.....71

Chapter 1: Introduction

Dilute nitrides have stirred great interest in the past ten years with their potential for applications as the active region material in light sources for telecommunications fiber-optic networks. By tuning the composition of the dilute nitride alloys, it is possible to achieve light emission in the wavelength range of 1.3 - 1.55 μm which is the window of interest in fiber-optic telecommunications. This chapter will provide an overview of the current demands for the latest generation of fiber-optic networks, examine the available III-V alloy materials, introduce the material of choice for this work and contrast it to other existing alternatives. Finally, I will explain the role of Transmission Electron Microscopy (TEM) in understanding and improving the alloy semiconductors for lasers.

1.1 Requirements for Modern Fiber-Optic Networks

We begin this section by providing an overview of the structure of a modern fiber-optic network. There are two main components to such a network: the Network Backbone and the Network Access ports shown in Figure 1.1. The Network Backbone is the long-haul part of the telecommunications network. For example, this could be the fiber lines connecting two distant metro areas, i.e. San Francisco and New York. The preferred transmission wavelength for the long-haul part is 1.55 μm since the silica fiber has its lowest loss at this wavelength

and data is transmitted over large distances. Currently, there is sufficient capacity built-up for the long-haul networks to meet the rapidly increasing voice and data traffic. As such, the long-haul network can be compared to a multi-lane highway where the traffic is flowing smoothly and there are no bottlenecks. The situation is quite different for the Network Access ports of a fiber-optic network. Network Access can be a Metro Area Network (MAN) or Local Area Network (LAN) and in terms of the road analogy it can be viewed as the entrance/exit ramps from a highway or, in more dramatic terms, as a dirt road connecting a highway to a local neighborhood. This part is typically a true bottleneck and new sources are needed to increase its bandwidth.

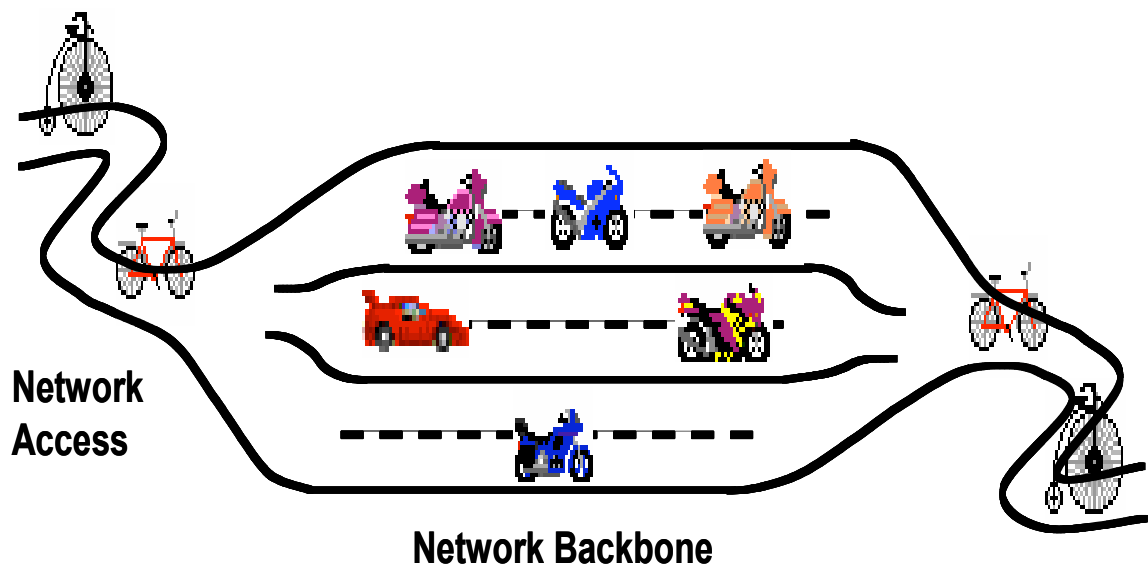


Figure 1.1: Schematic of a typical fiber-optic telecommunications network [1].

Before we discuss the higher capacity need for the Network Access ports imposed by the great increase in data traffic in the last years, let us examine in more detail the transmission wavelengths of interest in a fiber-optic telecommunications network. Figure 1.2 shows a diagram of the dependence of fiber loss on the transmission wavelength for today's silica fiber.

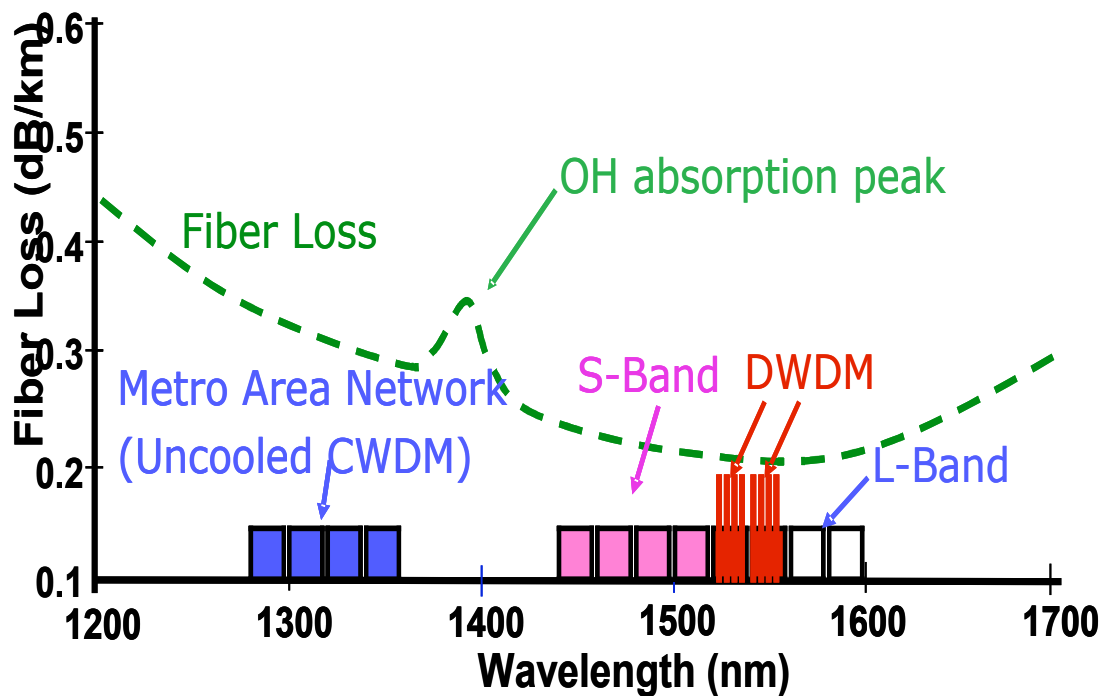


Figure 1.2: Dependence of fiber loss on transmission wavelength in the silica fiber [1].

The diagram above shows that there are two windows of opportunity for low loss transmission separated by a high OH absorption peak. The lowest loss window is centered around 1.55 μm . The red region shows the currently used bandwidth in the modern Dense Wavelength Division Multiplexing (DWDM) network architecture. The sources that emit at these wavelengths are well-

developed and have been used for the past two decades. We see that on both sides of this region there is additional bandwidth that is not currently utilized due to the limited gain region of Erbium Doped Fiber Amplifiers (EDFAs) and lack of suitable sources that can emit at these wavelengths. The second window is centered around 1.3 μm . This is a region of relatively higher loss but nonetheless is adequate for use in LANs and MANs where the transmission distances are not large. There are currently no sufficiently low cost sources that can provide the tens to hundreds millions lasers that are required for widespread deployment of high bandwidth MANs and LANs. There is thus a great need for the development of new, low cost, 1.3 – 1.6 μm lasers in order to utilize the available bandwidth.

The need to develop new sources for MANs and LANs has become more pressing in the last years as higher and higher data transmission speeds are demanded by the new generation of data networks. Figure 1.3 shows the dependence of transmission distance on the transmission bit rate in a silica fiber [2,3].

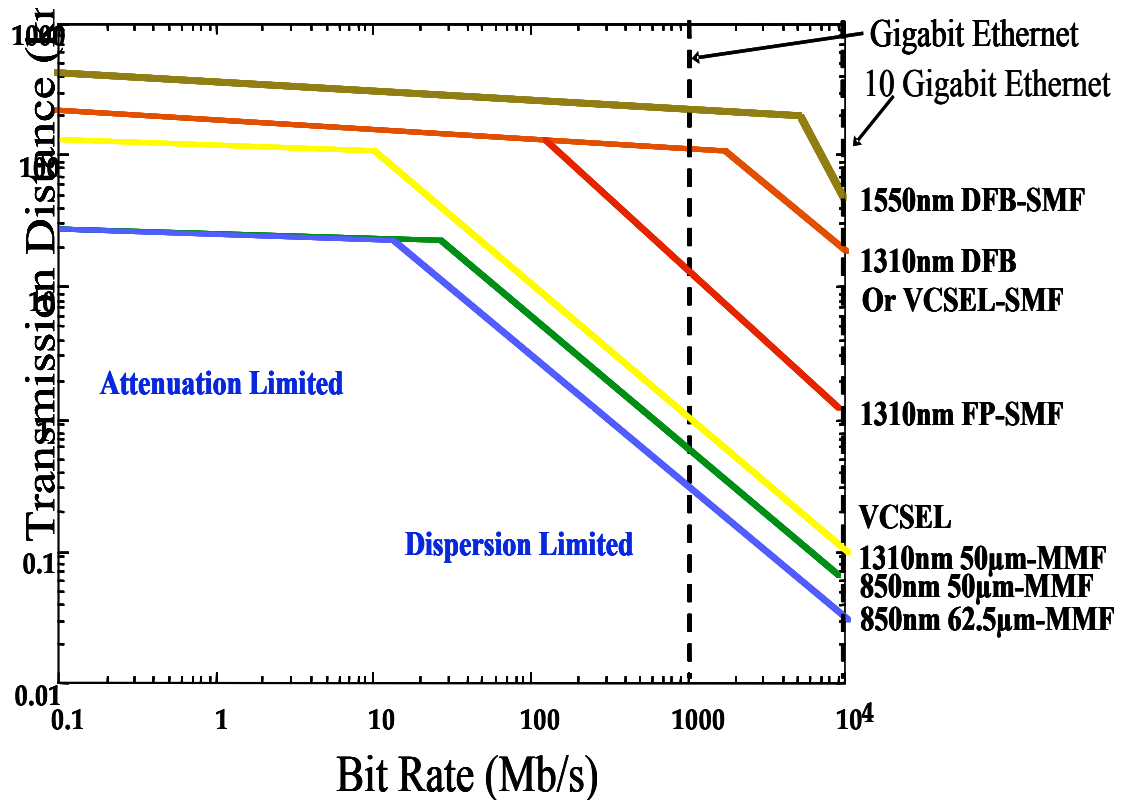


Figure 1.3: Dependence of the transmission distance on the transmission speed [2].

We see that the transmission distance falls off dramatically as the bit rate increases above 100 Mbps. Let us focus our attention on the line in Figure 1.3 that shows the dependence for a laser source emitting at 850 nm. This is a very well-developed source based on GaAs that has been widely used in the past decade. We see that for this laser, the transmission distance is on the order of a few kilometers at 100 Mbps transmission speed, which is quite adequate for a LAN. This is no longer the case for a present-day network with transmission speed of up to 10 Gbps. We see that in this case the transmission distance falls

off to several tens of meters, which is no longer sufficient, even for a small intra-building LAN. The solution to this dramatic decrease in transmission distance is to increase the transmission wavelength. Figure 1.3 shows that a laser at $1.3\ \mu\text{m}$ has transmission distance of several kilometers even at a speed as high as 10 Gbps. This explains very well why it is critical to develop longer wavelength low cost sources in order to enable very fast (up to 10 Gbps) LAN and MAN networks.

1.2 Material Choices for Long-Wavelength Emission

In this section, we will examine the available material choices among the existing III-V alloys. Figure 1.4 shows the bandgap versus lattice parameter dependence for the well-known applicable III-V compounds. The two horizontal lines across the diagram indicate the bandgaps that correspond to emissions at 1.3 and $1.55\ \mu\text{m}$. We will focus our attention on alloys grown on GaAs and InP.

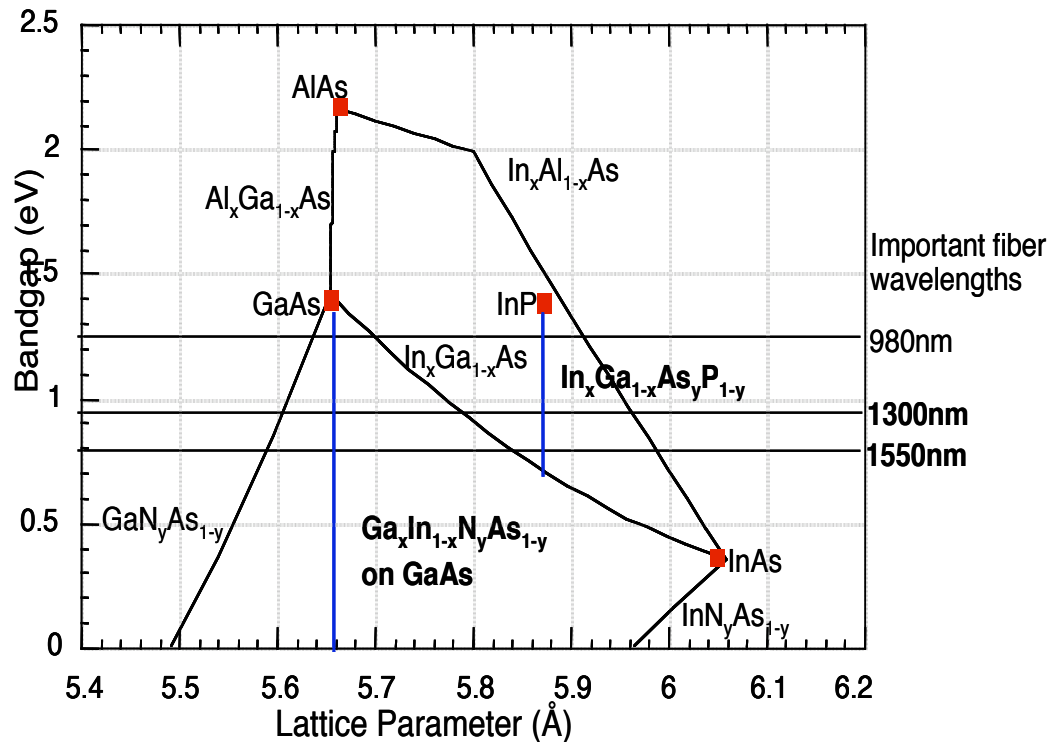


Figure 1.4: Bandgap dependence on the lattice parameter for some important III-V alloys [4].

The choice for the currently employed lasers in the long-haul networks emitting at 1.55 μm , is the InGaAsP alloy grown on InP wafers. However, this material has fundamental limitations that preclude its use in low cost applications [5]. We will discuss the limitations for the use of this material in MANs and LANs later in this section. Let us first focus our attention on alloys that are based on GaAs. The diagram shows that GaAs has a bandgap that corresponds to emission at 850 nm. Clearly, if we are to extend the emission out to 1.3 μm and further, we need to make use of some suitable smaller bandgap alloy. There are two possible alloying constituent shown in the diagram: indium and nitrogen. The

bandgap of the alloy resulting from the combination of two binaries (a ternary alloy) is shown as the lines connecting the binaries in the diagram. Let us look at the line connecting the GaAs and InAs binaries, which models the behavior of the InGaAs ternary alloy. We see that by adding indium to GaAs, it is possible to increase the emission wavelength but at the same time we also increase the lattice parameter of the resulting alloy. This is undesirable with respect to growing high quality single crystal material on GaAs. The large lattice mismatch between GaAs and the InGaAs alloy would result in dislocations and other crystal defects, which decrease the luminescence efficiency of the material and the lifetime of lasers. To avoid this, we have to add a fourth constituent which would serve to decrease the lattice mismatch and allow the growth of single crystal material lattice matched to GaAs. We accomplish this by adding nitrogen to the ternary InGaAs alloy. It turns out that nitrogen also helps to further red shift the emission wavelength. This is very counter-intuitive and its discovery by Kondow et al [6-9] created great interest in this alloy and stimulated vast research to explore its potential for long-wavelength emission. GaN has a smaller lattice parameter and larger bandgap than GaAs, so it was expected that adding nitrogen to GaAs would reduce the lattice parameter and increase the bandgap. Contrary to this expectation, nitrogen decreases both the lattice parameter and the bandgap. This is a very fortunate circumstance because by adding nitrogen to InGaAs, we are able to achieve both lattice matching and a red shift in the wavelength to the desired 1.3 μm and beyond. The reason for this counter-intuitive behavior lies in the nature of the nitrogen atom: it is very small and has

high electronegativity. Due to these properties, adding nitrogen to GaAs creates a localized defect level above the conduction band minimum which forces the bandgap lowering because the conduction band can not intersect this localized N level (known as antiband crossing) [10]. This results in a very large bandgap bowing which translates into a simultaneous increase in the emission wavelength and decrease in lattice parameter. Thus by adding nitrogen and indium to GaAs, we are able to control both the emission wavelength and the lattice parameter. This enables us to red shift the emission wavelength out to 1.3 μm while simultaneously preserving lattice-matched conditions and growing high crystalline quality GaInNAs material on GaAs.

At this point we would like to compare the GaInNAs alloy with its main competitor for long-wavelength emission: the InGaAsP alloy grown on InP. This comparison will be done in the context of a particular laser structure known as the Vertical Cavity Surface Emitting Laser (VCSEL), first reported in 1979 by Iga [11] at the Tokyo Institute of Technology. VCSELs will almost certainly be the choice for sources in future low cost high-performance fiber-optic networks due to their inherent advantages over competing edge emitting laser structures. Figure 1.5 shows a schematic of a typical VCSEL structure.

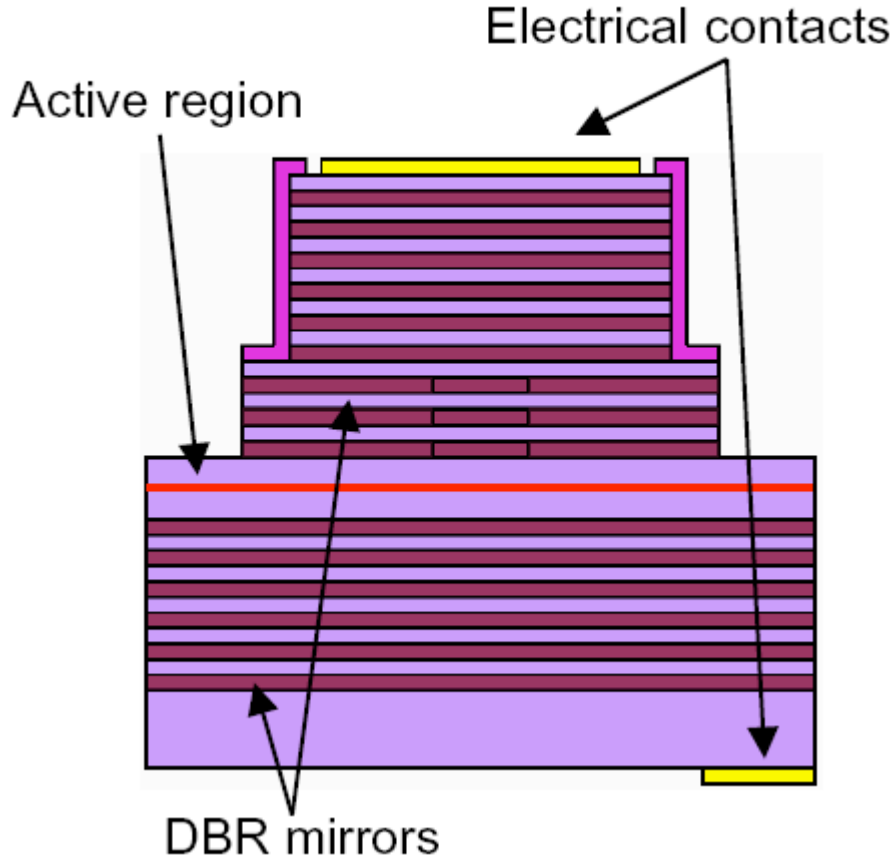


Figure 1.5: Schematic of a VCSEL structure [12].

In a VCSEL structure, the mirrors are parallel to a thin active region and light travels perpendicular to the mirrors through the active layer. VCSELs are preferred over more conventional edge emitting laser structures because of their much lower cost and ease of coupling to fiber. Their unique design allows devices to be manufactured and tested on a single wafer and greatly simplifies the coupling of the fiber to the device [13]. The vertical structure also enables very space-efficient network architectures which are critical in LANs. Lasing in a

VCSEL is achieved through a combination of quantum well optical gain region and pairs of quarter-wavelength mirrors, which consist of alternating semiconductor layers with different refractive index. These are known as Distributed Bragg Reflector (DBR) mirrors. Since the active layer in a VCSEL is typically very thin, amplification and lasing are greatly dependent on the mirrors, and thus it is crucial to have a suitable material system where alternate layers with different composition can be grown with high refractive index contrast.

In terms of the above outlined requirements for a VCSEL structure, GaInNAs wins over InGaAsP as a better material choice for VCSEL fabrication. GaInNAs beats InGaAsP on four major criteria: 1) Cost, 2) DBR mirrors, 3) Operating temperature and 4) Thermal conductivity.

Growth on GaAs is a well-established and mature technology. In contrast, InP wafers are more expensive and growth on InP is considerably more difficult. It is typically characterized by difficult compositional control and consequently lower yields. Thus, lasers based on GaInNAs grown on GaAs are very low cost, which is a critical requirement for a LAN network where the number of laser sources required can be very large.

GaInNAs-based VCSELs have the advantage of a readily available DBR mirror technology. It is based on alternating GaAs/AlAs quarter-wavelength mirror layers which can be grown lattice-matched and have high refractive index contrast. Thus, to achieve the high reflectivity required for the mirrors (greater than 99.9%), around 25-30 mirror pairs are needed. In the InP-based system, similar quarter wave mirrors require 60 pairs and any absorption precludes

achieving adequately high reflectivity. For example, the InGaAsP/InP and AlGaInAs/AlInAs mirror systems require more than 50 mirror pairs to achieve similar reflectivity. These also have poorer thermal conductivity since they are based on ternary and quaternary alloys as opposed to the GaAs/AlAs binaries. This fact, coupled with the greater number of mirror pairs that are required, makes the fabrication of VCSELs based on InP very challenging and prohibitively expensive.

A third advantage to the GaInNAs VCSELs is the better temperature characteristic of these devices [14,15]. This is due to the intrinsic electronic properties of the GaInNAs/GaAs heterojunction. A number of theoretical and experimental studies have shown that most of the band offset at the heterojunction occurs in the conduction rather than the valence band. [9,16,17]. This results in a relatively large conduction band offset $\Delta E_c = 0.7\Delta E_g$. This is very favorable since good confinement of the electrons in the conduction band is more critical to the device than the confinement of the holes in the valence band. This is due to the fact that the electrons have a smaller effective mass and it is easier for them to leak out of the quantum well when thermally excited. By comparison, the conduction band offset in the InGaAsP/InP system is much smaller. It has been estimated to be $\Delta E_c = 0.4\Delta E_g$ [18, 19]. Consequently, the properties of InP-based lasers (i.e. threshold current) are much more sensitive to temperature. As temperature increases, more and more electrons have the necessary energy to leak out of the well. This increases the Auger recombination rate and reduces the gain of the device. It is a run-away process which exacerbates with further

increase in the temperature. As a result of the unfavorable band offset, devices based on InP need to be operated under external cooling. This works fine for long-haul networks albeit at higher cost and increased space requirements for these devices. This is not a huge problem in a long-haul network where few sources are needed and thus their cost is a small fraction of the total fiber-optic network cost. It is a significant disadvantage in a LAN, where a greater number of sources is needed and the requirements for space are much tighter. Therefore a GaInNAs-based VCSEL is much better suited for these applications since it can be operated under ambient conditions.

1.3 Role of TEM in Understanding and Improving the Material

While GaInNAs is an excellent candidate for sources emitting at wavelengths in the range 1.3–1.55 μm , significant challenges must be overcome before the full potential of this alloy is realized.

One of the main challenges in growing this material is the very low solid solubility of nitrogen in the InGaAs alloy. As mentioned before, nitrogen is a unique atom in the sense that it has a very small atomic radius and high electronegativity. Thus, it is quite different from the other three constituents in the alloy and does not mix well with them. This places very unique requirements on the growth of these alloys. In order to overcome the very low solid solubility of nitrogen, these alloys are grown under metastable conditions. Growth is done with Molecular Beam Epitaxy (MBE) under low temperatures (around 450 $^{\circ}\text{C}$)

and with a very reactive atomic nitrogen plasma source. This allows us to incorporate up to a few percent nitrogen before phase segregation occurs. The downside to low temperature growth is the high amount of crystalline defects (interstitials, vacancies) that are incorporated in the material. In order to improve the crystalline quality, a post-growth anneal is necessary for this alloy.

Another challenge in the growth of material with uniform composition has been the presence of interaction effects between the gallium, indium and nitrogen atoms. Research in our and other groups has established that during the annealing stage, there is some rearrangement between the nitrogen atoms' nearest neighbors [20]. Specifically, the material changes from a configuration where the nitrogen has more gallium nearest neighbors before annealing (the normal statistical distribution for a gallium-rich alloy) to one where it has more indium nearest neighbors after annealing. The driving force for this rearrangement is the minimization of the bonding energy between the nearest neighbors. The practical effect on the material optical properties is a blue shift in the emission wavelength. This has complicated things further by having to design for this shift during annealing by adjusting the indium and nitrogen compositions.

The above-described characteristics make the growth of good quality GaInNAs material extremely challenging. As a result, GaInNAs samples often exhibit phase segregation and compositional fluctuations. Most of these challenges have been successfully overcome for GaInNAs that emits out to 1.3 μm , through improvements in the growth and annealing practices [7, 21-23]. Such material contains around 34% indium and 2% nitrogen. Extending the

wavelength beyond 1.3 μm out to 1.55 μm (which requires increasing the indium content up to 39%) had proven virtually impossible to achieve solely through growth and annealing improvements. Adding more indium to the alloy resulted in severe phase segregation and made it impossible to grow material with good optical properties [24]. Recently, the addition of small amounts of antimony during the growth has led to a dramatic improvement in the luminescence efficiency of the alloy and put it back on track for 1.55 μm emission [2, 25-29].

It was already mentioned that phase segregation and compositional non-uniformities are the main roadblocks on the way towards better optical quality material. In terms of real device performance, compositional fluctuations have been blamed for broad emission spectra, low gain and high threshold currents in devices [30]. It is clear that achieving uniform composition in this material system is key to dramatically improved device performance.

A lot of the improvements that were achieved via growth optimizations and the addition of antimony were only registered through measurements of the optical qualities in the material. There was not a lot of understanding of the structural changes in the material that were responsible for these improvements. This thesis describes extensive application of various Transmission Electron Microscopy (TEM) techniques in order to gain an understanding of the fundamental structural changes that occur at the atomic level, which are believed to be responsible for the significant improvements in the optical properties of the material. While there is an array of different structural characterization techniques, i.e. X-ray Diffraction (XRD) and Secondary Ion Mass Spectroscopy (SIMS), the

majority of those are macroscopic techniques where the information is averaged over large areas of the sample. On the other hand, TEM is very powerful in investigating phenomena at the local atomic level. Because of this, TEM is the main focus of the work in this thesis as the best tool to study the phase segregation behavior and compositional fluctuations in the GaInNAs(Sb) alloy.

Chapter 2: TEM Techniques

This chapter will cover the different TEM techniques used in this work to structurally characterize GaInNAs(Sb) quantum well structures. Each technique will be presented through some theoretical background and the relevant results from the investigation of the GaInNAs(Sb) material. The four TEM techniques that will be covered are: 1) High Resolution Imaging (HRTEM), 2) Energy-Filtered imaging (EFTEM), 3) Energy-Dispersive X-ray Spectroscopy (EDX) and 4) Dark-Field Imaging (DF).

2.1 Cross-Section TEM Sample Preparation

This section begins with a presentation of the basic sample structure used in the TEM experiments. This structure is known as a cross-sectional TEM sample. Figure 2.1 shows a schematic of this sample.

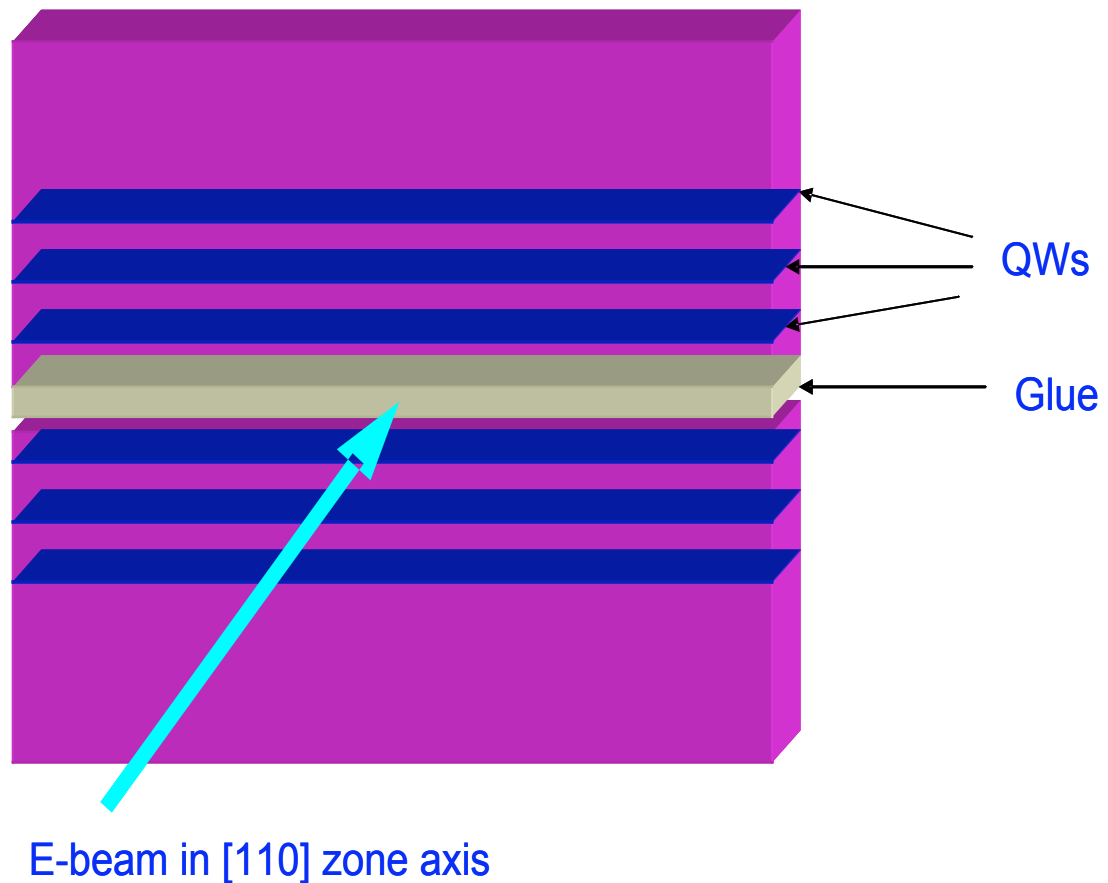


Figure 2.1: Configuration for cross-section TEM sample with the electron beam along the [110] zone axis.

The diagram above (not to scale) shows two pieces of GaAs wafer glued together to form an integral sample. This is known as the “sandwich” technique and the sample is prepared in the (110) orientation. The active quantum well regions consisting of the GaInNAs(Sb) alloy are shown as the blue planes in the diagram. This particular diagram shows a structure with three quantum wells but samples with a single quantum well were also used. The arrow illustrates the direction of the electron beam in the microscope. In the sample orientation shown,

the electron beam is perpendicular to the quantum wells and is along an orientation known as the [110] zone axis.

This type of cross-sectional TEM sample is prepared by cutting and gluing together two pieces of the same GaAs wafer. The sample is then thinned by mechanical grinding with diamond paper. Progressively smaller paper grits are used in successive steps to achieve thinning and polishing at the same time. A rough 30 micron grit paper is used initially for the initial mechanical grinding. Finer grits of 15 and 6 microns are used to further thin and polish the sample. The final polishing step utilized 1 micron grit paper, which produces a finely polished sample surface and a final sample thickness of approximately 20-30 microns.

The final sample preparation step involves putting the sample in an ion mill where very fine polishing of the surface is achieved through energetic Ar⁺ ions, which bombard the surface at a shallow angle (usually 5 – 6 degrees). The ion milling is done at two different ion energies. In the first step, 5 keV Ar⁺ ions are used to thin the sample to electron transparency (around 10 nm thick). This is done in a conventional Gatan ion mill. The final step involves a very fine polishing step with 1 keV Ar⁺ ions which was done to achieve exceptionally smooth surfaces for the microscope investigation. This was done in a unique ion mill in the Lawrence Berkeley National Laboratory (LBNL) at the National Center for Electron Microscopy (NCEM). In addition to being able to produce Ar⁺ ions with very low energy, this ion mill also has a low temperature milling capability by using liquid nitrogen. Low temperature milling was used for all the samples

investigated in this study since it helps to improve the surface smoothness. This, combined with the low ion energy and shallow milling angles, enabled us to prepare samples with exceptional surface smoothness and quality. This was crucial for the high resolution part of the TEM investigation where the generation of readily interpretable high resolution images was highly dependent on the sample surface quality.

2.2 High Resolution Imaging (HRTEM)

This section will describe the fundamentals of High Resolution TEM (HRTEM) imaging and will present the results from this analysis for the GaInNAs(Sb) structures. HRTEM is a widely used technique and is probably the most involved in terms of sample preparation, image generation and image interpretation. This work uses HRTEM in the conventional sense to generate the images but employs a novel technique in the image interpretation. The HRTEM images were used to generate strain maps over the quantum well regions of the GaInNAs(Sb) samples in order to extract information about the compositional uniformity of the material in the quantum wells. This procedure and the method will be presented in detail later in this section.

Figure 2.2 presents the sample configuration in relation to the electron beam in HRTEM imaging.

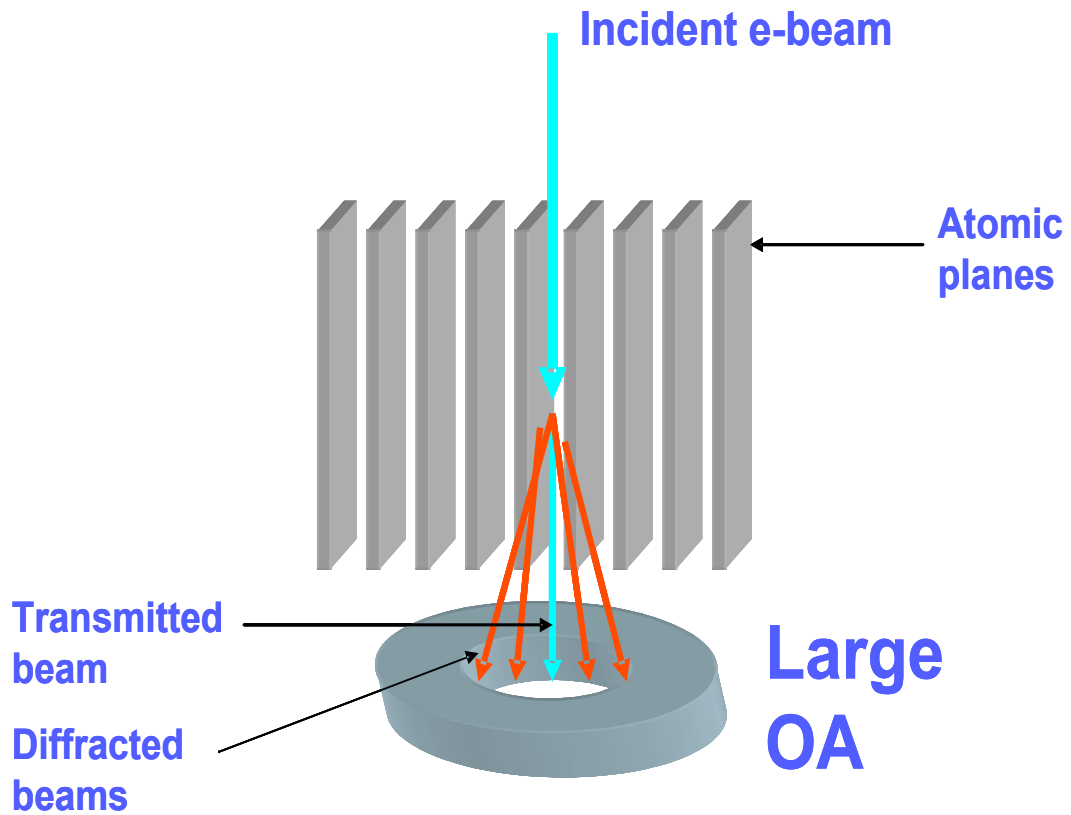


Figure 2.2: High Resolution (HRTEM) imaging configuration.

The diagram above shows that in the HRTEM imaging configuration, the atomic planes are oriented parallel to the incident electron beam in the microscope. This orientation produces a strong transmitted beam and a multitude of diffracted beams from the different sets of atomic planes that are parallel to the incident beam. This is sometimes counterintuitive to researchers who are mainly involved with X-ray diffraction analysis, where the requirement for diffraction is that the X-ray beam be oriented at a Bragg angle to the diffracting planes. In

electron microscopy, due to the high electron energy and the resulting very short wavelength of the electrons, appreciable diffraction results even from atomic planes that are not oriented at a Bragg angle to the incident beam. This is a tremendous advantage because it allows reconstructions of the crystal lattice to be obtained almost instantaneously and from a single sample orientation. The multitude of beams diffracted from the planes parallel to the incident beam are collected with a large objective aperture (OA) in the microscope and it is the interference of these beams that generates an image which is essentially a reconstruction of the crystal lattice.

Figure 2.3 shows the typical HRTEM image that is obtained from the GaInNAs(Sb) quantum well structures.

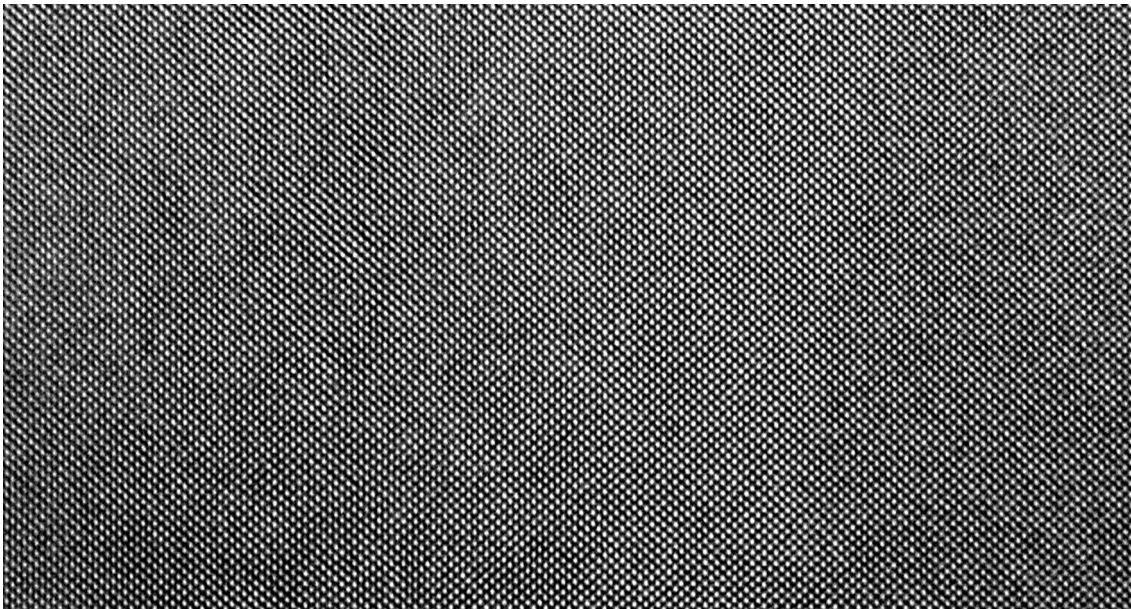


Figure 2.3: HRTEM image of the quantum well area of a GaInNAs sample.

The image above clearly shows the atomic planes and the peaks can be interpreted as the positions of the individual atoms. This image is of very high quality over a large sample area, which includes all three quantum wells and the barriers between them. The very smooth sample surface and high image quality were the result of the low energy (1 keV) ions, shallow angles and low temperature during the ion milling process. This high quality is critical for the strain mapping analysis which will be presented later in this section.

Another peculiarity that merits consideration is the fact that these images were obtained in a very high voltage electron microscope. This is a unique facility located at the LBNL NCEM and the operating voltage of this microscope is 800 kV. It is a JEOL microscope with 0.15 nm nominal resolution. The images were obtained on photographic plates for the best possible resolution. In addition to better resolution, there is a far more important reason for using a very high voltage machine. The samples under investigation in this work contain highly strained quantum well regions which tend to relax when the sample is thinned down to electron transparency. A general rule of thumb is that the area under investigation has to be thicker than the quantum well width in order to avoid significant relaxation. The nominal well width in our samples is 8 nm. With a higher voltage beam, we are able to penetrate thicker areas of the sample (around 10 nm and above) while still maintaining sufficiently high resolution. Thus, the use of higher voltage electrons is critical in obtaining a true representation of the strained quantum well regions. Next, we will outline the procedure for generating a strain map from the HRTEM images.

Strain mapping is performed on the HRTEM images in several steps. First, an area of interest containing the quantum well is selected from the HRTEM image. Next, the selected area image is filtered to subtract the diffuse background intensity and make the peaks (which can be interpreted as the positions of the atoms) more defined. These two steps are shown in Figures 2.4 and 2.5.

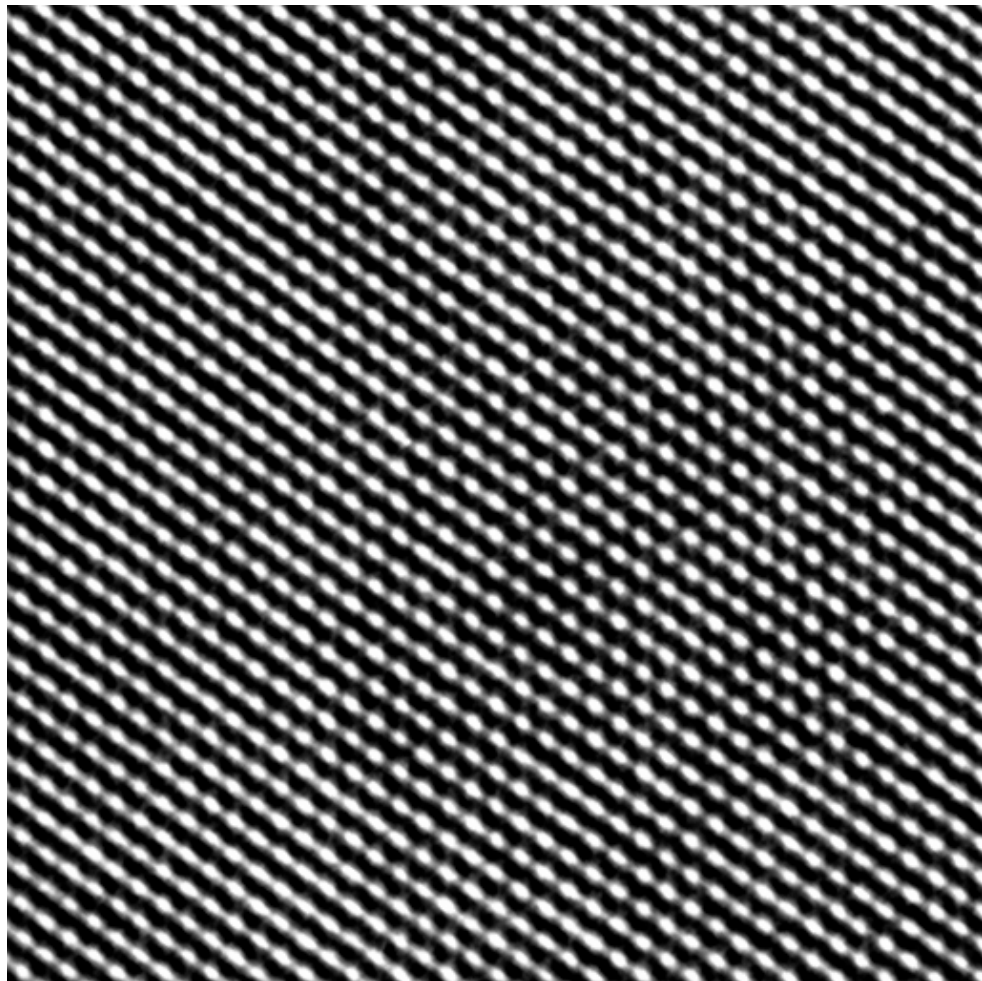


Figure 2.4: Selection of the original HRTEM image.

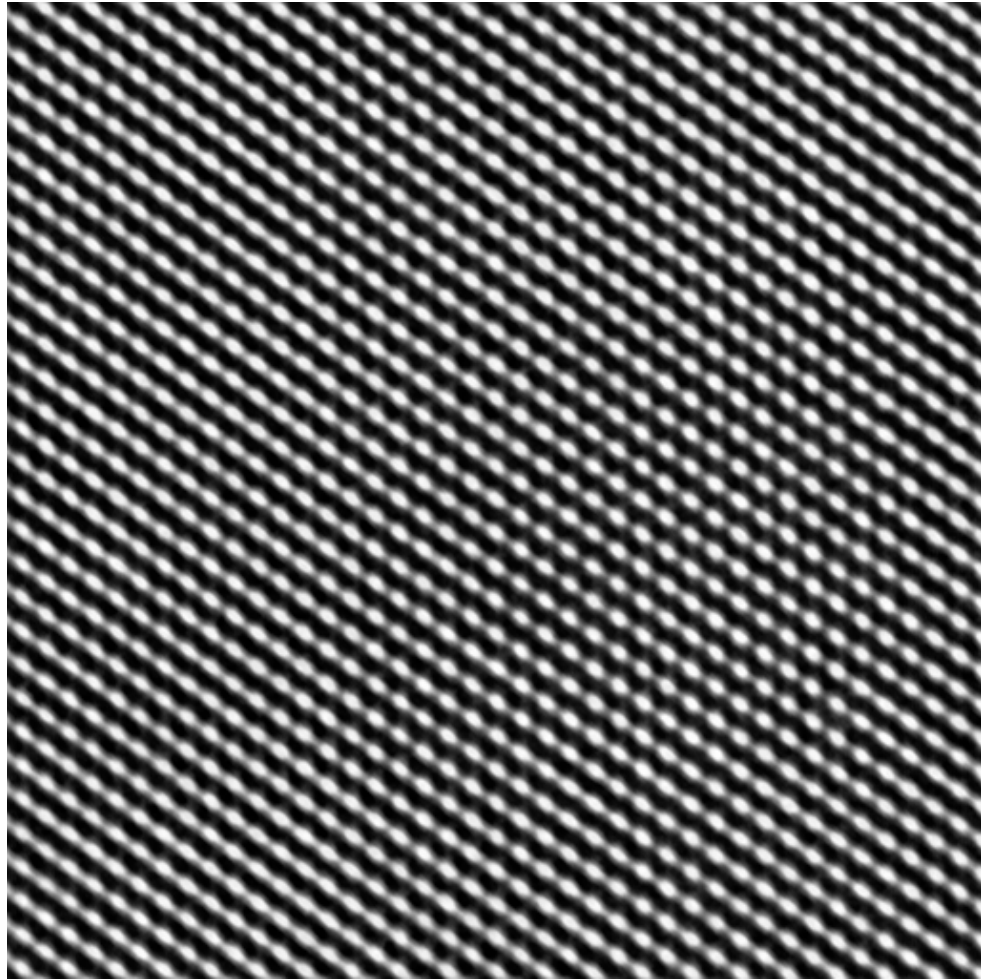


Figure 2.5: Filtered image.

Following the filtering step, strain maps are generated from the high resolution lattice images using the DARIP program developed at the National Center for Electron Microscopy (NCEM) at the Lawrence Berkeley National Laboratory (LBNL) in Berkeley, California. This is done through the following procedure. The DARIP program is used to identify and mark the peaks in the

filtered image. Next, a lattice is defined by the user by choosing several of the peaks. The lattice selection is random and usually the most convenient lattice is chosen. Based on this initial unit cell selection by the user, DARIP calculates a lattice which it then locks to the peak positions in the image. Images of the peak and lattice fitting procedures performed by the DARIP program are shown in Figures 2.6 and 2.7.

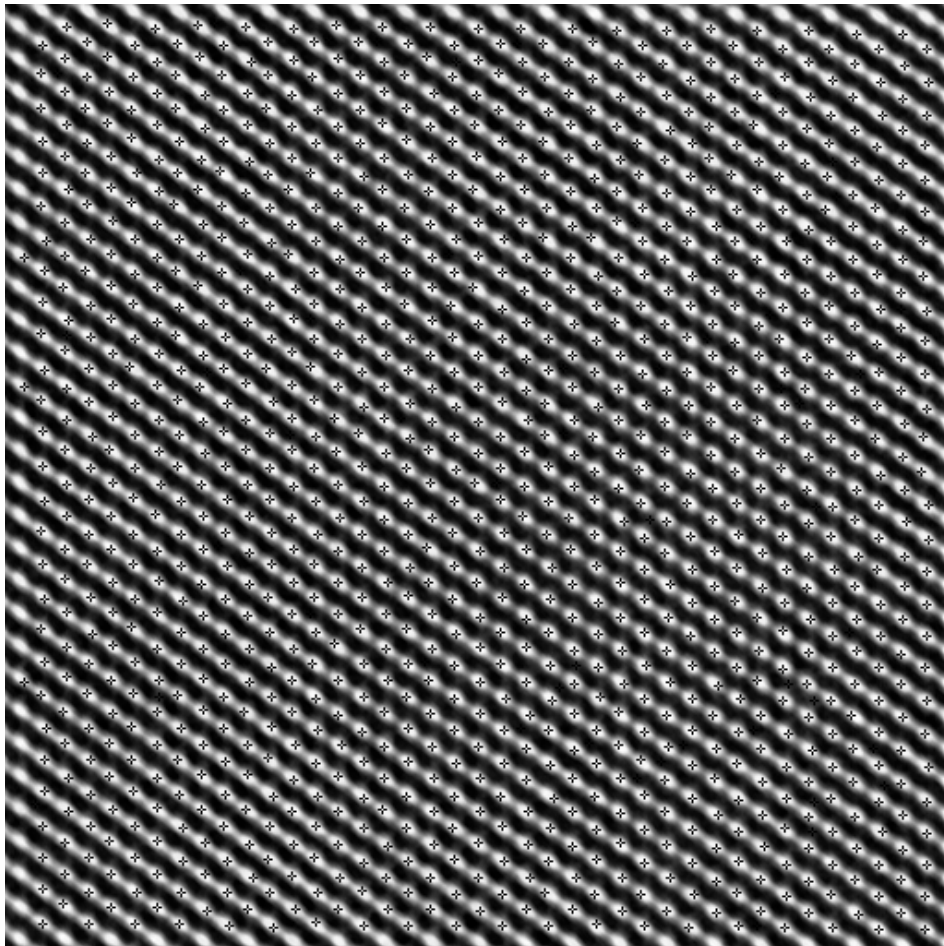


Figure 2.6: Filtered image with fitted peaks.

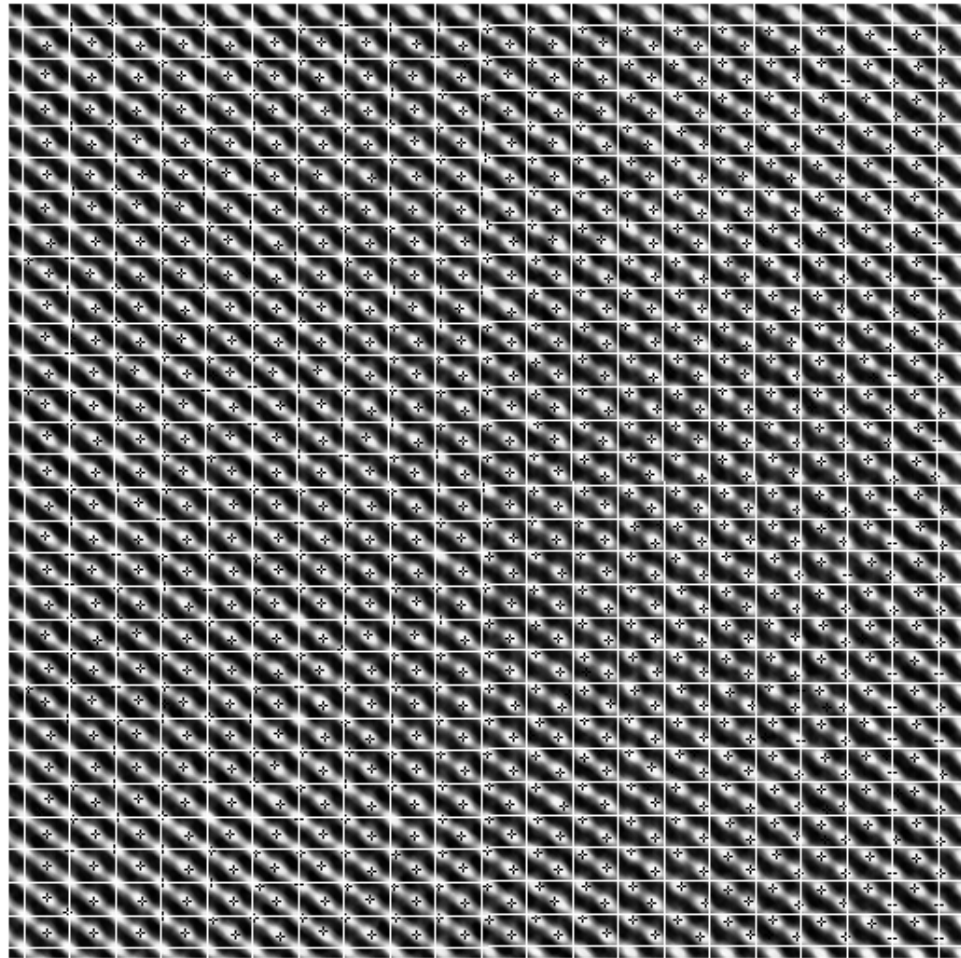


Figure 2.7: Filtered image with fitted lattice.

The lattice spacings from the lattice-fitted image are then extracted and a strain map is generated, which is essentially a map of the lattice parameter over the selected area. A typical strain map of this kind is presented in Figure 2.8.

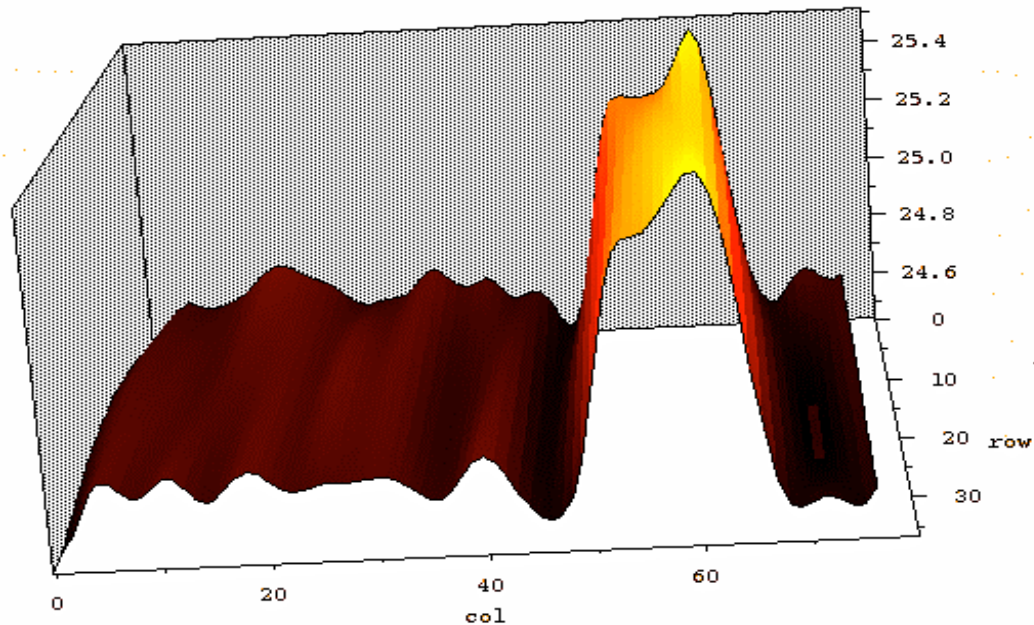


Figure 2.8: Strain map across a single quantum well GaInNAs sample.

The strain map in the image above is for a single quantum well (QW) GaInNAs sample with a nominal composition of 30% indium and 1.6% nitrogen designed for 1.3 μm emission. The nominal width of the quantum well is 8 nm. The sample was investigated in the un-annealed state. In the strain map image above, the single quantum well clearly appears as a peak due to the fact that indium, being a larger atom than gallium, swells the lattice; the higher the indium concentration, the greater the lattice distortion. Figure 2.8 shows clearly that the indium concentration profile is very asymmetric. It consists of two bumps with the

higher indium concentration occurring near the top interface of the well, providing evidence that indium segregates near the top of the well. This is very undesirable since there are effectively two different indium compositions in the well, which would broaden the emission spectrum. The difference in the rear and leading edge compositions was estimated to be around 8%.

In order to verify that there is no relaxation occurring in the strained quantum well region, we performed a calculation of the expected strain in the well for an active material with the above composition. The out-of-plane strain in the well is defined as follows:

$$\varepsilon_{out - of - plane} = \frac{a_{004} - a_{eq}}{a_{eq}} \quad (2.1)$$

where a_{004} is the strained out-of-plane lattice parameter and a_{eq} is the unstrained equilibrium lattice parameter. The relationship between a_{004} and a_{eq} is determined by the GaInNAs film stiffness coefficients C_{12} and C_{11} as follows:

$$a_{eq} = \frac{2 \frac{C_{12}}{C_{11}} a_{GaAs} + a_{004}}{1 + 2 \frac{C_{12}}{C_{11}}} \quad (2.2)$$

where a_{GaAs} is the lattice parameter of the GaAs matrix. The ratio $2 C_{12}/ C_{11}$ is around 0.9 for the majority of III-V materials [31]. From Vegard's law, we calculated a_{eq} for GaInNAs with 30% indium and determined a_{004} through the relationship in Equation 2.2. Thus, we calculated an expected out-of-plane strain value of 1.9% for 30% indium composition. From a measurement on the strain map, we obtain an experimental value for the out-of-plane strain of 1.6% for the

same sample. This is within the ballpark of the expected strain value considering that our theoretical strain calculation does not account for the nitrogen in the well (nitrogen, being a smaller atom, would reduce the lattice parameter and strain value a bit). Thus, we believe that there is no significant strain relaxation in the wells as a result of the TEM sample preparation.

Figure 2.9 shows the strain map for a GaInNAs(Sb) sample which has a nominal composition of 38% indium, 1.6% nitrogen and 2% antimony in the wells and 2.3% nitrogen and 6% antimony in the GaNAsSb barriers. This sample has three quantum wells with nominal width of 8 nm. The GaNAsSb barriers between the wells have a nominal width of 20 nm.

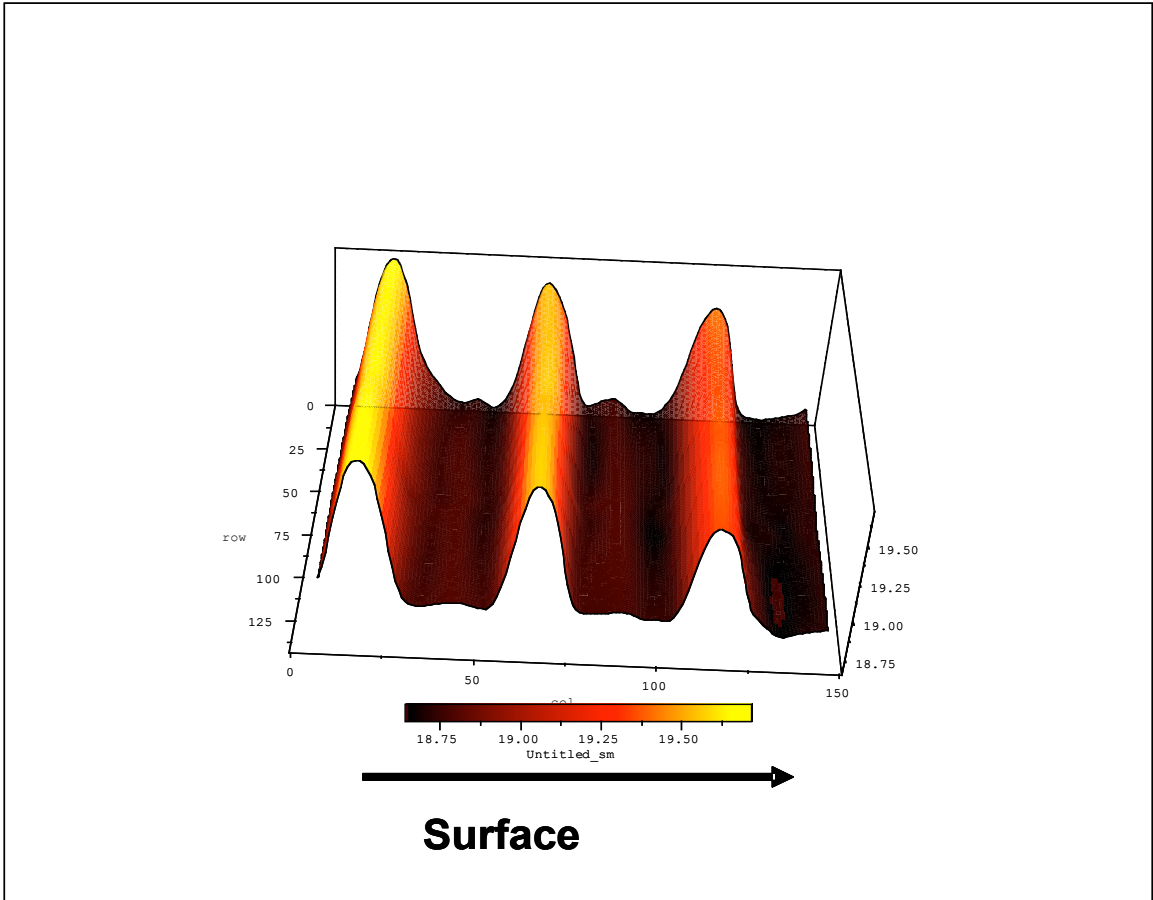


Figure 2.9: Strain map of a triple quantum well GaInNAs(Sb) sample.

The strain map above shows great improvement in the uniformity of the profiles across the quantum wells compared to the GaInNAs sample shown in the first strain map (Figure 2.8). This improvement is attributed to the addition of antimony during the growth, since otherwise the two samples were grown under identical conditions. The compositional profiles are very smooth and do not display any of the signs of phase segregation as in the case of the GaInNAs sample. The peak height decreases from the bottom to the top well, which likely

indicates decreased indium incorporation. The variation of the indium concentration between the wells is roughly 4%. This is likely due to some heating that occurs during subsequent well growth. The wells have a smaller bandgap than the GaAs substrate and absorb more heat, which effectively raises the growth temperature and leads to decreased indium incorporation. Another possibility is that strain accumulates with an increasing number of wells (especially if the barriers are not under tensile strain to provide strain compensation) which would also decrease the indium incorporation. It is clear that growth adjustments would be necessary to counteract these effects.

Figures 2.10, 2.11 and 2.12 show extended strain maps along each of the wells of the GaInNAs(Sb) sample in order to examine the compositional uniformity within the wells.

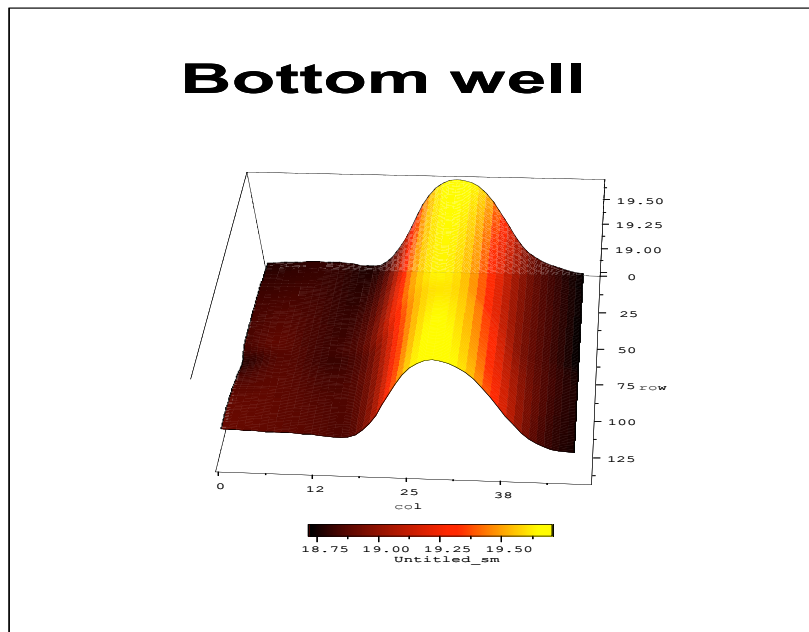


Figure 2.10: Extended strain map along the bottom well of GaInNAs(Sb).

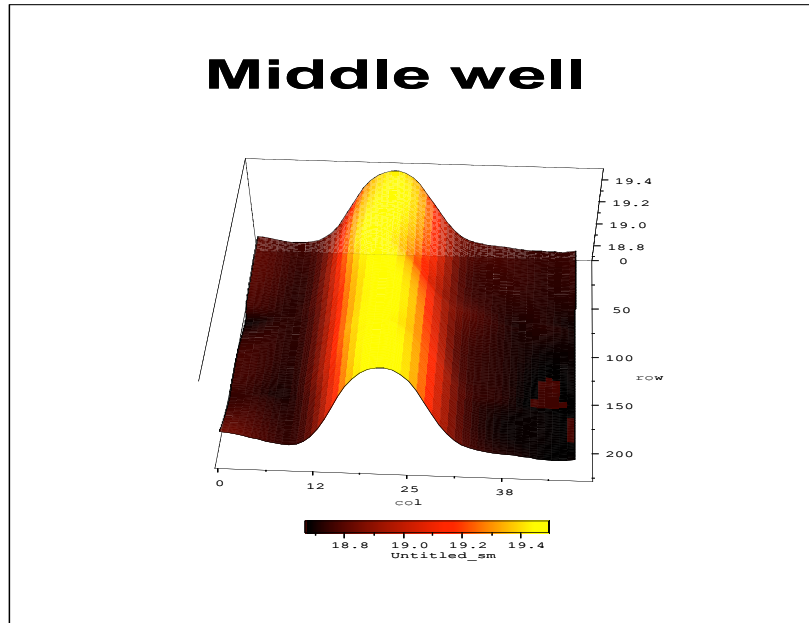


Figure 2.11: Extended strain map along the middle well of GaInNAs(Sb).

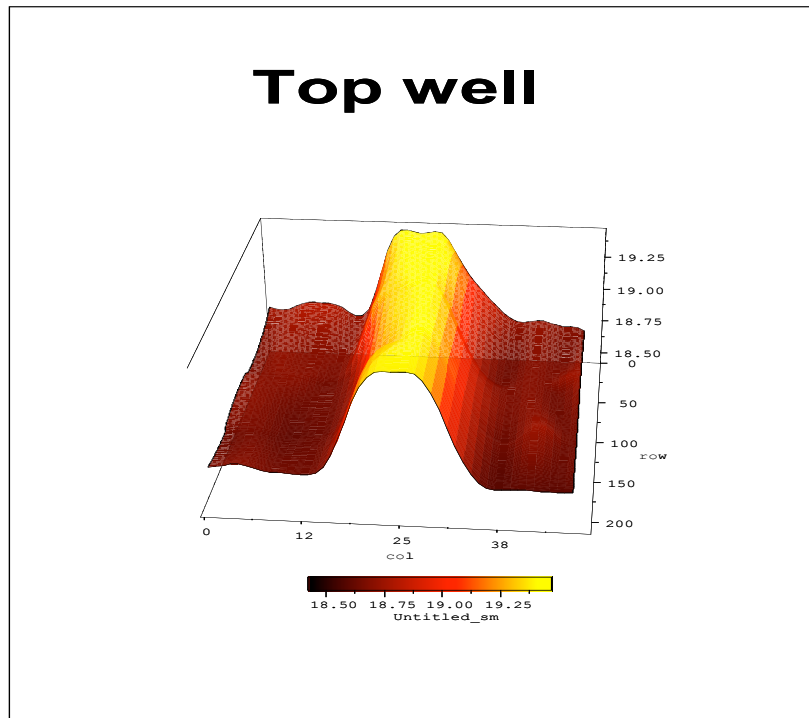


Figure 2.12: Extended strain map along the top well of GaInNAs(Sb).

For the extended strain maps above, it should be emphasized again that overall these appear much more uniform than the GaInNAs quantum well due to the beneficial effect of the antimony. Figures 2.10-2.12 show that the uniformity deteriorates somewhat from the bottom to the top well. The last well shows some indium clustering with a segregation distance of 20-30 nm, but this is not nearly as severe as with GaInNAs. This is probably due to the same effects described above, namely heating and strain accumulation during growth which promotes phase segregation.

Having discussed the great benefit of the antimony in improving the compositional uniformity as observed from the TEM images, it is worthwhile to take the time and discuss the mechanism through which antimony interacts with the lattice. Our best hypothesis at this point is that antimony mainly acts as a reactive surfactant. During the growth, antimony atoms adsorb on the crystal surface and form actual bonds with the crystal. In this position, they are able to grab adsorbed atoms of the other constituents and lock them in place. This greatly inhibits the surface mobility of the other constituent atoms (particularly indium) and prevents them from clustering and initiating three dimensional growth. So effectively antimony acts to stabilize the two dimensional plane-by-plane growth mode and thus improves the compositional uniformity and promotes smooth and sharp quantum well interfaces.

In order to correlate the structural findings from the strain maps to the optical qualities of the material, Photoluminescence (PL) and Cathodoluminescence (CL) measurements were performed on the GaInNAs and

GaInNAs(Sb) samples. In PL, a light source is used to excite electrons from the valence into the conduction band. When these electrons recombine with the holes in the quantum well region, they emit light which is then measured in a spectrometer. A series of PL spectra for both GaInNAs and GaInNAs(Sb) samples is shown in Figure 2.13.

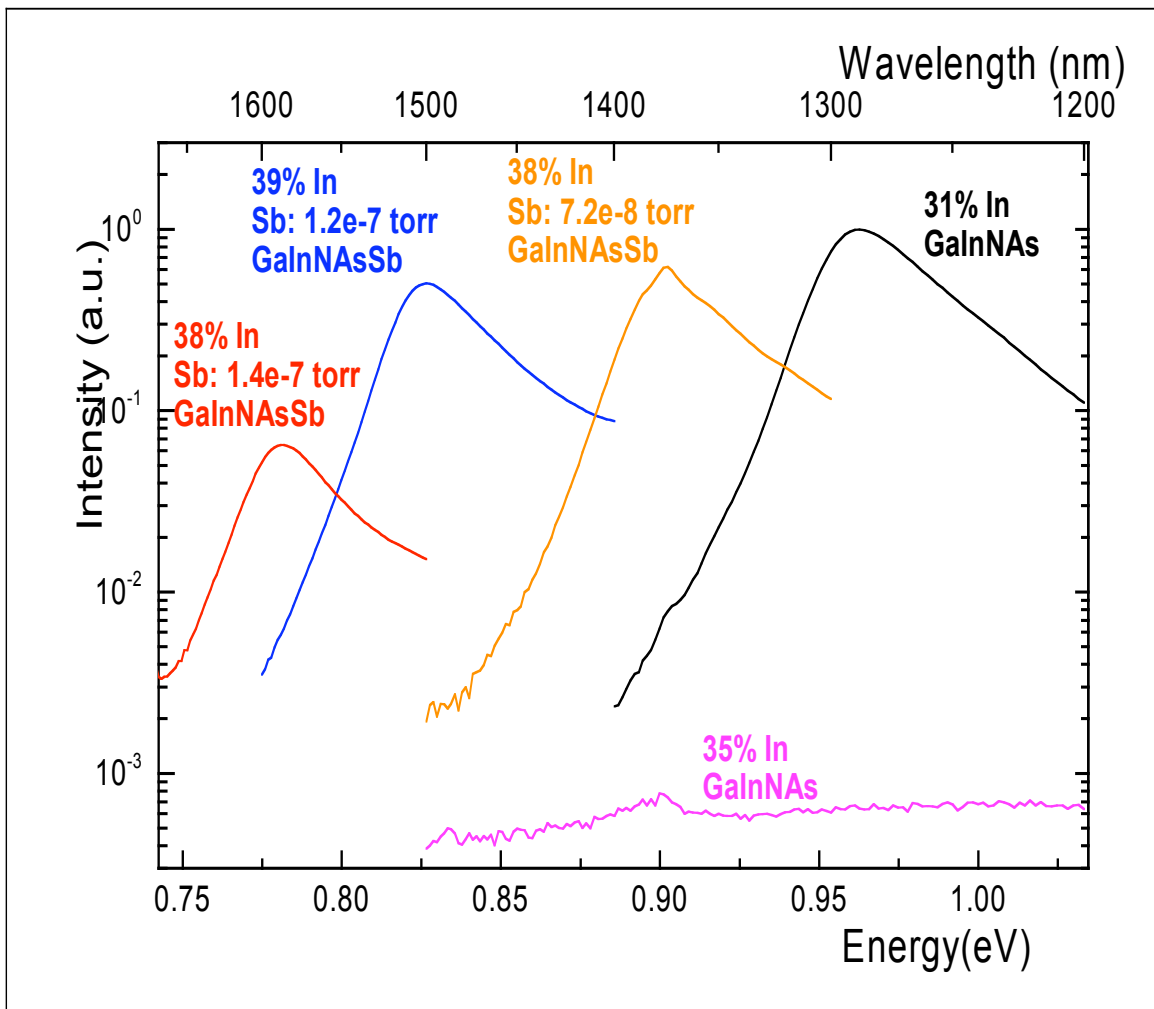


Figure 2.13: Photoluminescence spectra of GaInNAs and GaInNAs(Sb) samples.

The rightmost spectrum shows the PL for a GaInNAs sample containing 31% indium and designed for 1.3 μm emission. The spectrum at the bottom is the PL for a sample containing only a few more percent indium (35%). We see that these additional few percent of indium come at a very high cost: they effectively destroy all the luminescence from this sample. This is due to severe three dimensional growth and phase segregation. The figure shows that simply by including antimony in the growth we recover all the luminescence in a sample containing 38% indium. Antimony allows us to grow a sample with good luminescence with as much as 39% indium and emission out to 1.5 μm . These results are in excellent agreement with the strain maps which showed that structurally, antimony acts to improve the compositional uniformity of the material.

The Cathodoluminescence (CL) measurement is done in a Scanning Electron Microscope (SEM) where the electrons are excited with the electron beam and emit light upon recombining with the holes in the valence band. The powerful feature of this technique is that the beam can be rastered across the sample and a map of the compositional uniformity across the sample can be obtained. Figure 2.14 shows CL spectra for different GaInNAs and GaInNAs(Sb) samples [32].

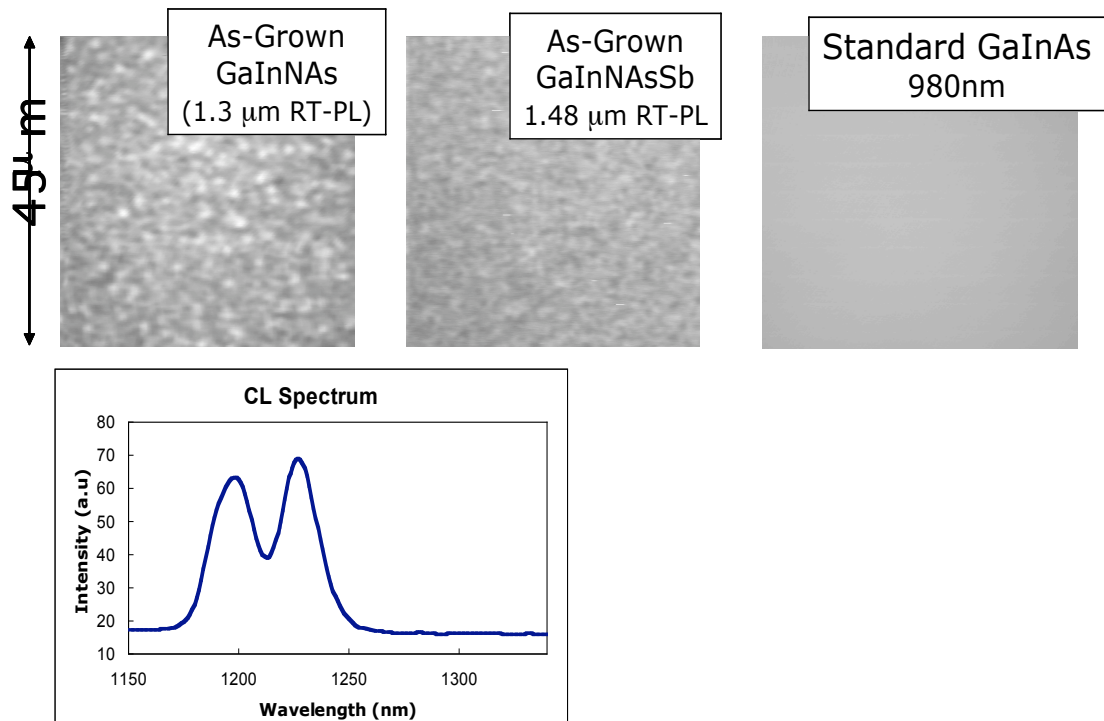


Figure 2.14: Cathodoluminescence spectra of GaInAs, GaInNAs and GaInNAs(Sb) samples [32].

The rightmost image in Figure 2.14 shows the CL spectrum for a standard GaInAs sample. Without any nitrogen, this sample emits light with wavelength of 980 nm. It is well established that GaInAs samples can be grown with a very high degree of material uniformity. This is well evidenced by the CL spectrum which displays very uniform contrast. The image to the left shows the CL spectrum for a GaInNAs sample designed for 1.3 μm emission. As expected, the image contrast is very spotty, providing evidence of extensive non-uniformity and phase segregation in the material. An analysis of the light spectrum in this image

(bottom rectangle) shows that it consists of two separate peaks which are emissions from areas with two different compositions. This is very reminiscent of the strain map for the GaInNAs sample which showed phase segregation and two different compositions existing in the quantum well. The middle image shows the CL spectrum for the GaInNAs(Sb) sample and, as expected, it shows a less spotty contrast and improved uniformity. The CL spectra correlate extremely well with the strain map findings and confirm again that antimony plays an important role in improving the compositional uniformity of the material.

2.3 Energy-Filtered TEM (EFTEM)

Energy-filtered imaging is another powerful TEM tool that can be used to investigate the compositional uniformity, provide additional insight and support the strain map images. EFTEM is unlike other imaging techniques in that only electrons of specific energy are used to form the image. When electrons strike and penetrate through the sample, a fraction of them is scattered inelastically, losing a certain amount of energy. The energy loss is very specific and is characteristic of the atoms of the element which are responsible for the scattering event. This allows us to generate spatial maps across the sample of the element of interest. In this case, indium was mapped, in order to correlate its distribution to the one from the strain maps. The EFTEM images were obtained in a Philips CM-200 microscope equipped with Gatan GIF analyzer which can select electrons of specific energy. The images were recorded with a CCD camera with

1024 x 1024 pixels resolution. Figure 2.15 shows the indium map EFTEM image for a GaInNAs(Sb) sample and Figure 2.16 shows a line profile of the intensity across the image.

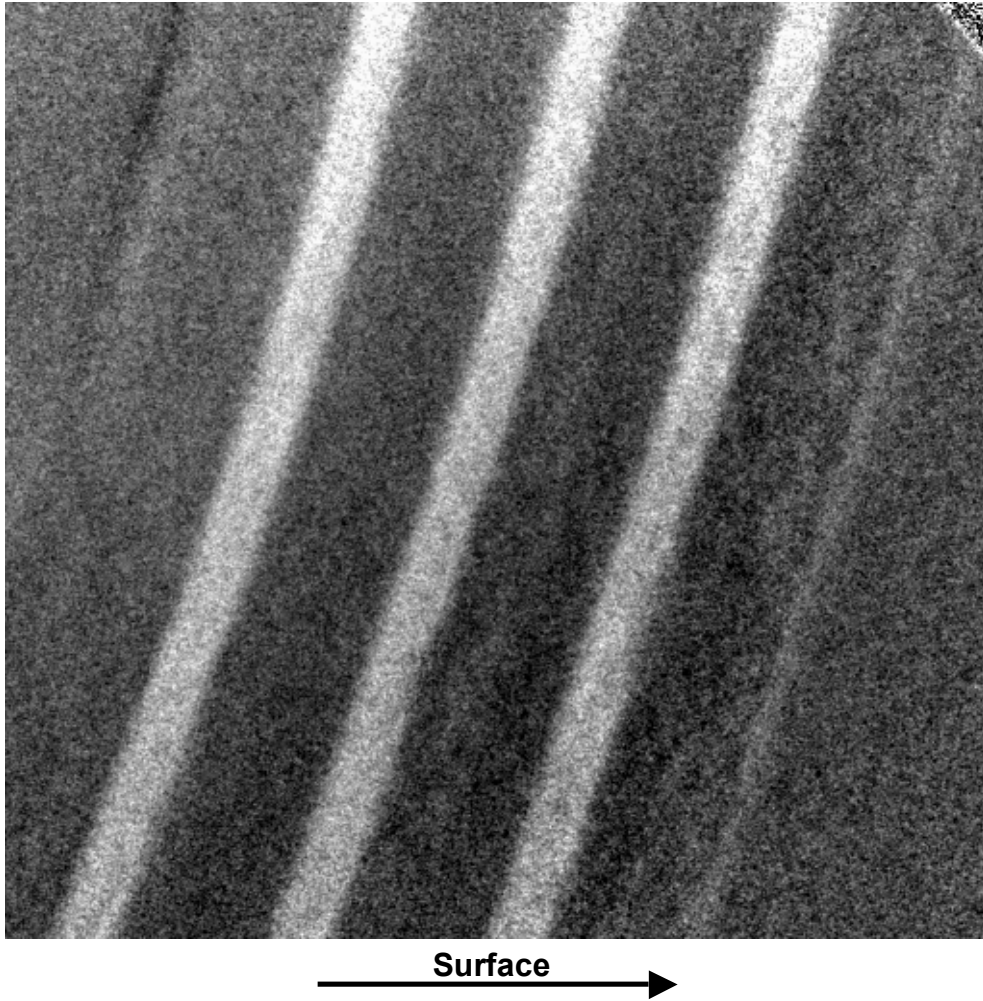


Figure 2.15: Indium EFTEM map of triple quantum well GaInNAs(Sb) sample.

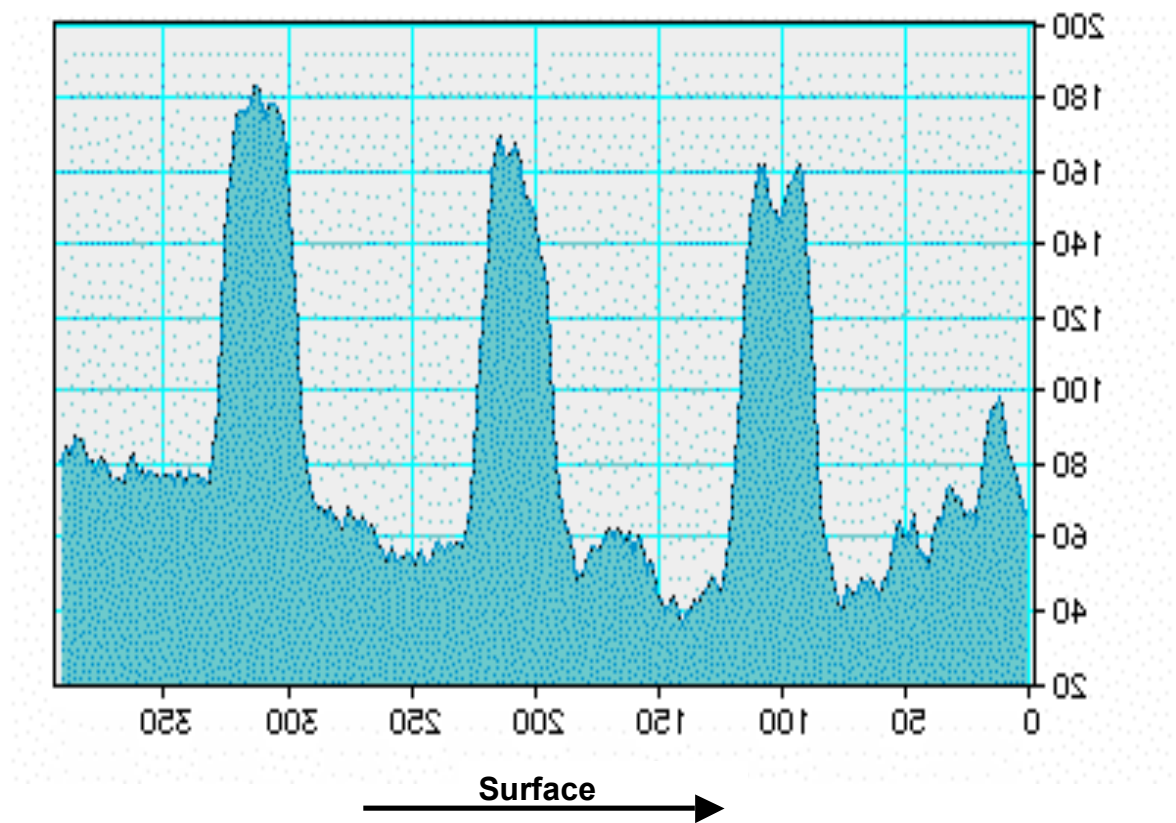


Figure 2.16: Intensity profile across the EFTEM image in Fig. 2.15.

In Figure 2.15, the contrast within the wells appears rather uniform which confirms that there is no significant indium clustering. The top well appears slightly more non-uniform than the other two wells, which is in excellent agreement with the extended strain maps along the wells. The intensity profile in Figure 2.16 reveals the same trend as the strain maps, namely the decrease in the indium concentration from the bottom to the top well.

2.4 Energy Dispersive X-ray Spectroscopy (EDX)

Energy dispersive X-ray spectroscopy is another technique that is very useful in mapping out elemental spatial distributions. The idea is similar to EFTEM, but this time element specific X-rays are used in the mapping rather than specific-energy electrons. In EDX, the electron beam is scanned across the sample and the X-rays that are generated in the process are analyzed with an energy spectrometer. The X-ray count from a specific element can then be plotted out and a line distribution for that element is generated. This technique has a relatively poor resolution which is determined by the smallest spot size achievable with the focused beam (the probe). For the microscope used in this study, the smallest probe size was around 2 nm. Despite the poor resolution, the technique is nonetheless very useful in identifying trends and correlating those to the other imaging techniques. The EDX images were obtained in a Philips CM-200 microscope equipped with an Oxford EDS detector. Figure 2.17 shows the EDX line profile for indium across the quantum well region in a GaInNAs(Sb) sample and Figure 2.18 shows the image of the sample area where the probe was scanned. Figure 2.19 shows the indium line profile for a single quantum well GaInNAs sample and Figure 2.20 shows the image of the area where the probe was scanned.

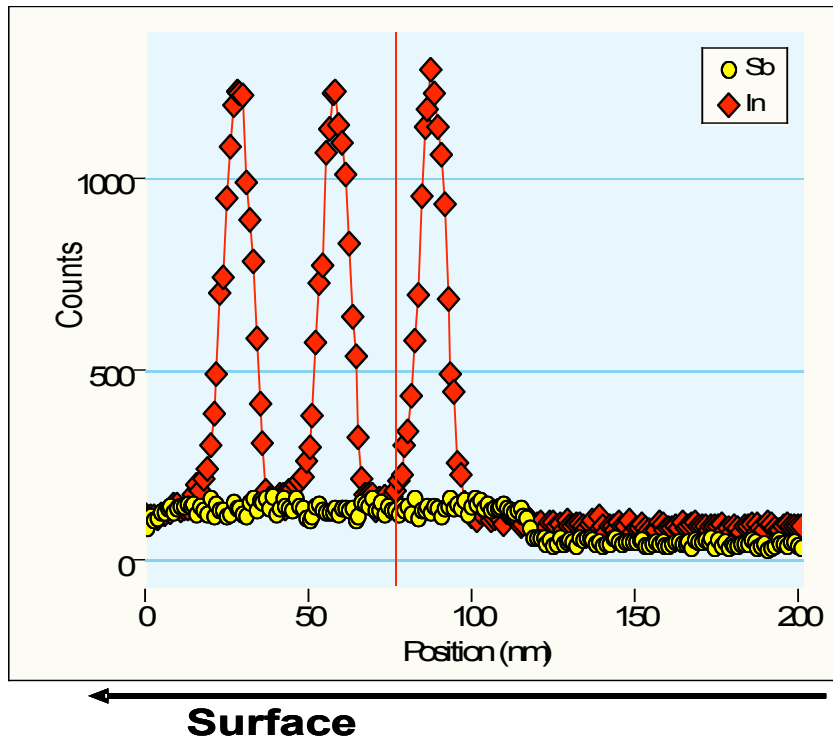


Figure 2.17: EDX spectrum across triple quantum well GaInNAs(Sb).

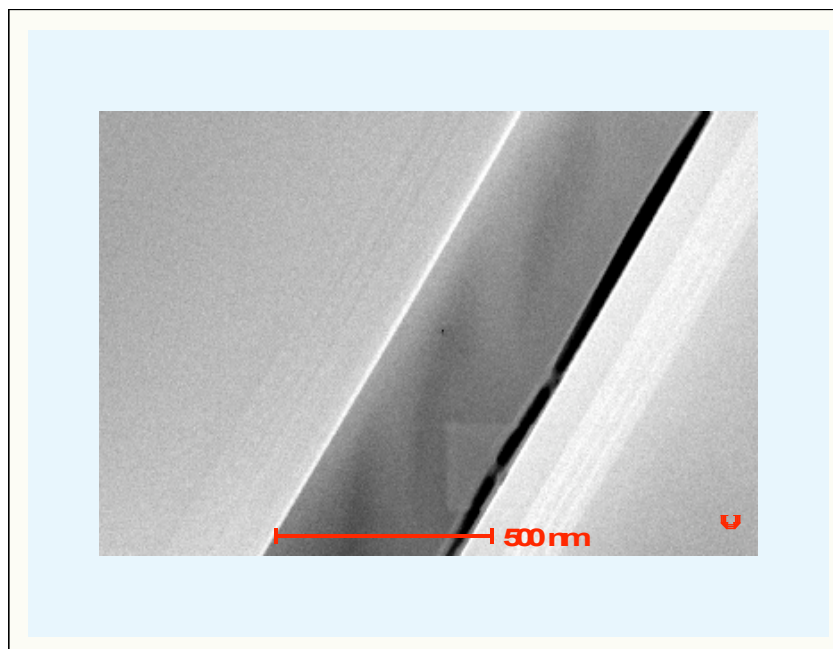


Figure 2.18: Image of sample area where the probe was scanned.

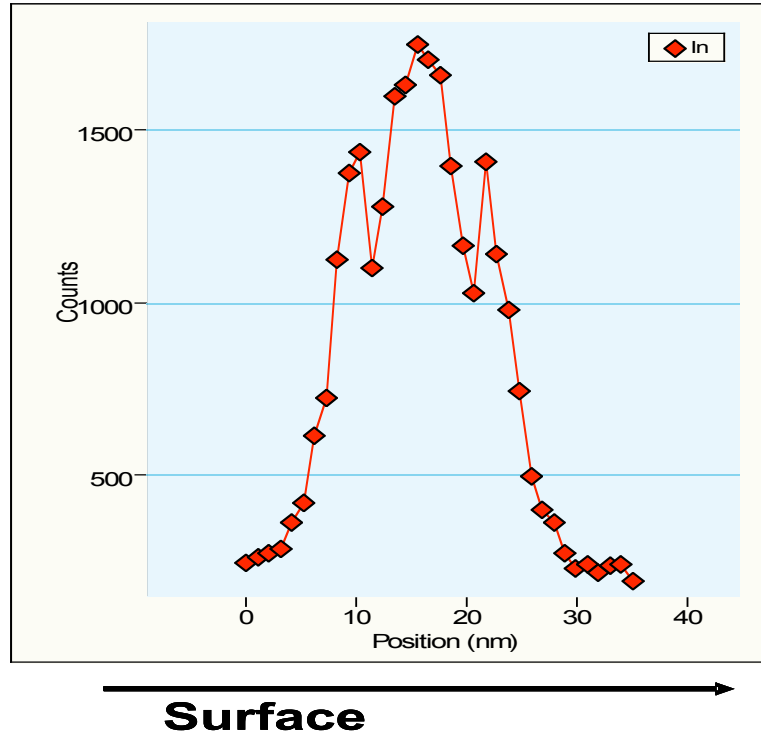


Figure 2.19: EDX spectrum across single quantum well GaInNAs.

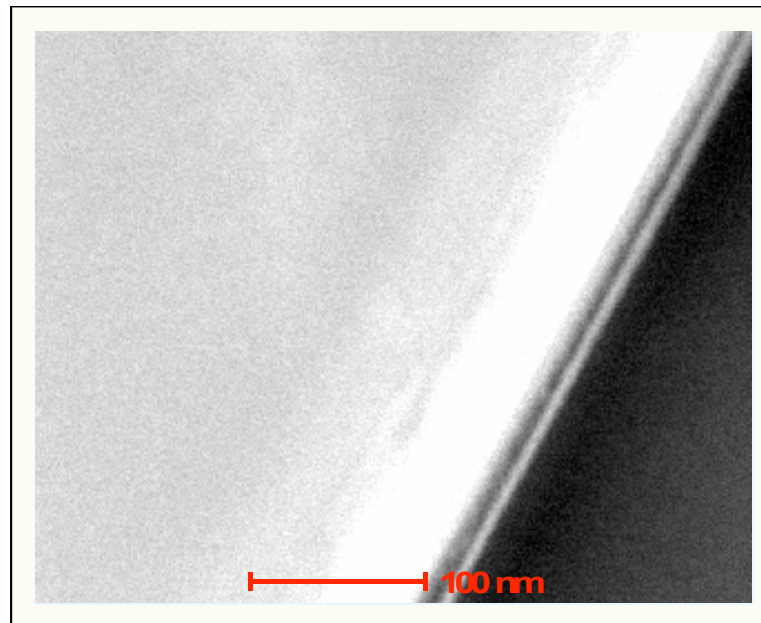


Figure 2.20: Image of sample area where the probe was scanned.

Figure 2.17 shows clearly the three quantum wells in the GaInNAs(Sb) sample which appear as pronounced peaks in the EDX image. The profiles are smooth and sharp which is in excellent agreement with the strain map. Figure 2.17 also reveals the same trend of decreasing indium concentration towards the surface although the decrease is not as dramatic as revealed by the strain map.

Figure 2.19 shows the indium profile across the single quantum well GaInNAs sample as an asymmetric and very non-uniform peak. Although the profile is broadened due to the poor resolution of the EDX technique (around 2 nm), it shows some evidence of indium segregation across the well, which is in very good agreement with the GaInNAs QW strain map.

2.5 Dark-Field (DF) Imaging

Dark-field imaging is very useful in obtaining information from specific sets of crystal planes. Depending on the orientation of the crystal planes, DF can be used to extract both strain and compositional information. Thus, it is extensively used in this work to reveal new information about the material and to complement the strain map analysis.

Figure 2.21 shows the typical sample-electron beam configuration in DF imaging condition.

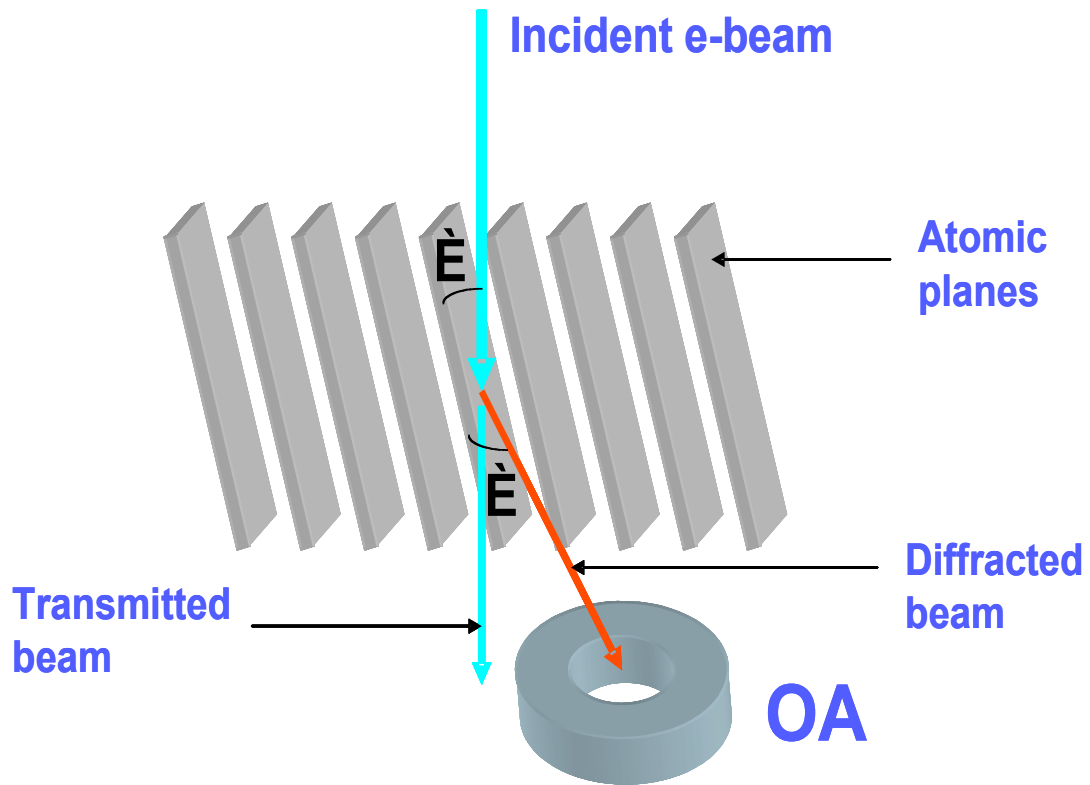


Figure 2.21: Dark-field imaging configuration.

The diagram above shows that in DF imaging, the crystal planes of interest are oriented at a Bragg angle to the incident electron beam. This results in a beam transformation that is quite different from the one in High Resolution imaging. Instead of a multitude of diffracted beams, the result is a transmitted beam and a single strongly-diffracted beam. The image is formed by selecting the strongly-diffracted beam with a small objective aperture in the microscope.

Depending on the particular set of crystal planes, the diffracted beam can reveal information about strain or composition in the material.

Figure 2.22 shows the $[110]$ zone axis diffraction pattern from the GaInNAs alloy (and any other III-V alloy).

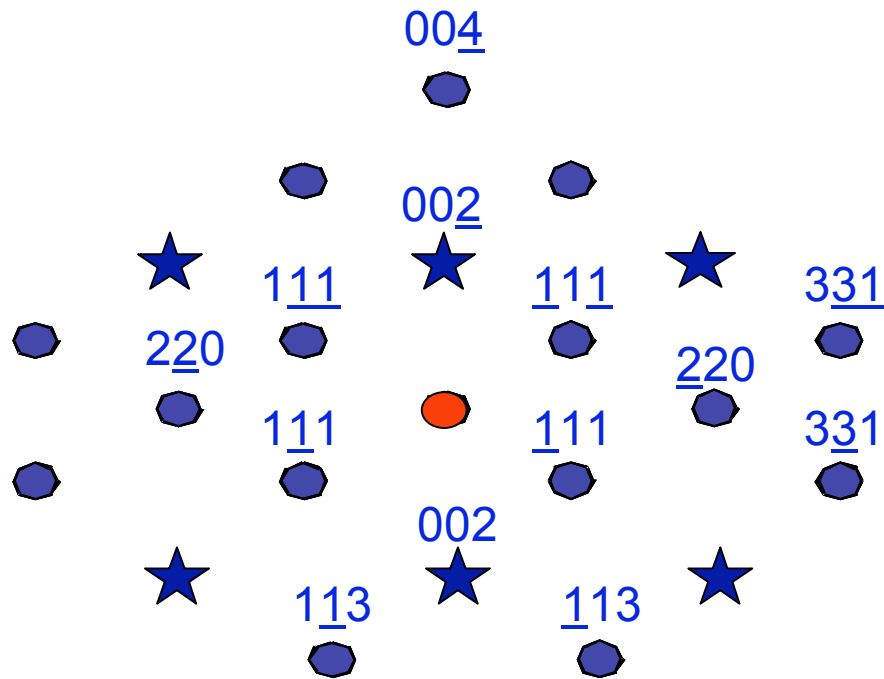


Figure 2.22: $[110]$ zone axis diffraction pattern.

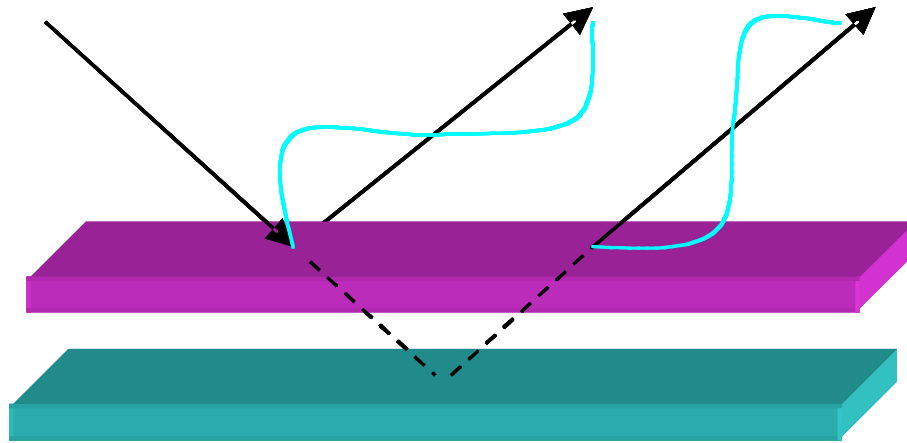
When the beam is aligned along the $[110]$ zone axis, it is parallel to all the planes in that zone. This is analogous to the High Resolution imaging configuration discussed earlier. A particular diffracted beam (reflection) can then be selected by tilting the sample and orienting those planes at a Bragg angle to the incident beam. This essentially extinguishes all other reflections and results

in a single strongly-diffracted beam. For example, orienting the (004) planes at a Bragg angle to the electron beam would result in a single strong (004) reflection in the diffraction pattern. The (004) diffracted beam is selected with the objective aperture and the image is formed containing information for the (004) planes.

Figure 2.23 shows the DF image for a single quantum well GaInNAs sample with the (004) reflection. The reciprocal vector \mathbf{g} for the (004) reflection is perpendicular to the (004) planes. Thus, the (004) reflection carries information about the (004) planes. Any variations in the spacing of these planes (due to strain or composition) will result in variations in the contrast of the (004) DF image. In Figure 2.23, the single quantum well in the GaInNAs sample shows up as a dark stripe on the lighter matrix background. The image shows considerable variation in the contrast, particularly near the top interface of the well. This is indicative of strain and compositional fluctuations within the well. The image is in excellent agreement with the strain map for the GaInNAs sample which showed segregation of indium at the top well interface.

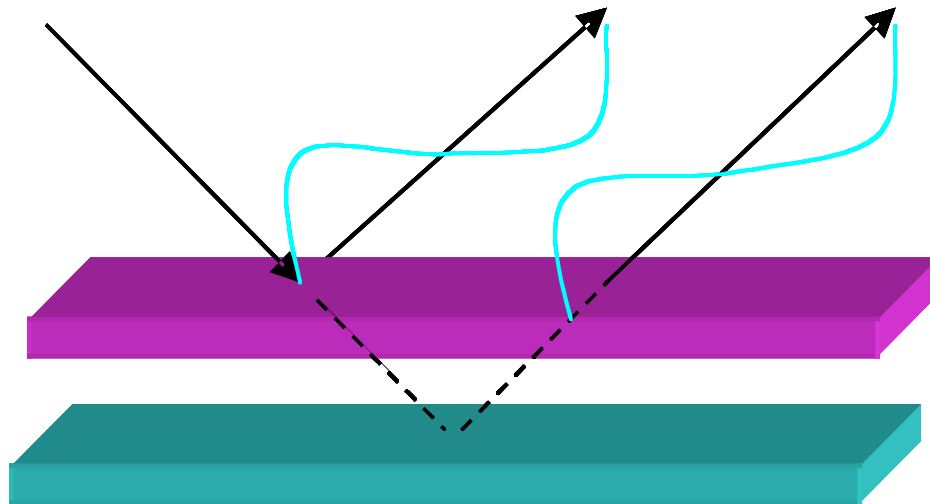
Figure 2.23: DF (004) image of a single quantum well GaInNAs sample.

The DF (002) reflection is very interesting and useful in the GaInNAs alloy since it is chemically sensitive. The nature of the (002) reflection is graphically illustrated and contrasted to the (004) reflection in Figures 2.24 and 2.25.



002 Condition

Figure 2.24: Schematic of the (002) imaging condition.



004 Condition

Figure 2.25: Schematic of the (004) imaging condition.

Figure 2.24 shows that in the (002) condition, the beams reflected off two different planes are exactly out of phase. Thus, in a structure with only one type of atom (such as the diamond cubic silicon), this reflection is completely extinguished and is not observed in the diffraction pattern. On the other hand, in a III-V alloy, the two planes shown in Figure 2.24 would consist of two different types of atoms (a plane of Group III and a plane of Group V atoms). Since different atoms have different scattering factors, the two reflected beams will not cancel each other exactly when they are out of phase. Consequently, the (002) reflection is sensitive to the compositional make-up of the planes. For the (004) reflection illustrated in Figure 2.25, the two reflected beams are precisely in phase. Thus, any variation in their intensity due to the different structure factors would be a small signal on top of the very large constructive interference signal. Due to this fact, the (004) reflection is not chemically sensitive in a III-V alloy.

The intensity of the (002) reflection has a square dependence on the difference between the composite structure factors of the group III and group V atoms and for the GaInNAs alloy is modeled as follows [33,34]:

$$I_{002} = A^2 = k^2 |f_{III} - f_V|^2 \quad (2.3)$$

$$f_{III} = x(f_{In} - f_{Ga}) + f_{Ga} \quad (2.4)$$

$$f_V = y(f_N - f_{As}) + f_{As} \quad (2.5)$$

where I_{002} is the (002) intensity, f designates the structure factors, x and y are the fractions of indium and nitrogen, respectively, and k is a constant.

Figure 2.26 shows the DF (002) image for a triple quantum well GaInNAs sample. In the image, the wells show up as stripes clearly delineated by dark lines. These occur at the well interfaces because the combination of the fractions x and y are such, that the reflection is completely extinguished. Within the wells, as the indium concentration increases, the (002) reflection is no longer extinguished and the brightness is recovered. Thus, a higher indium concentration will result in increased brightness.

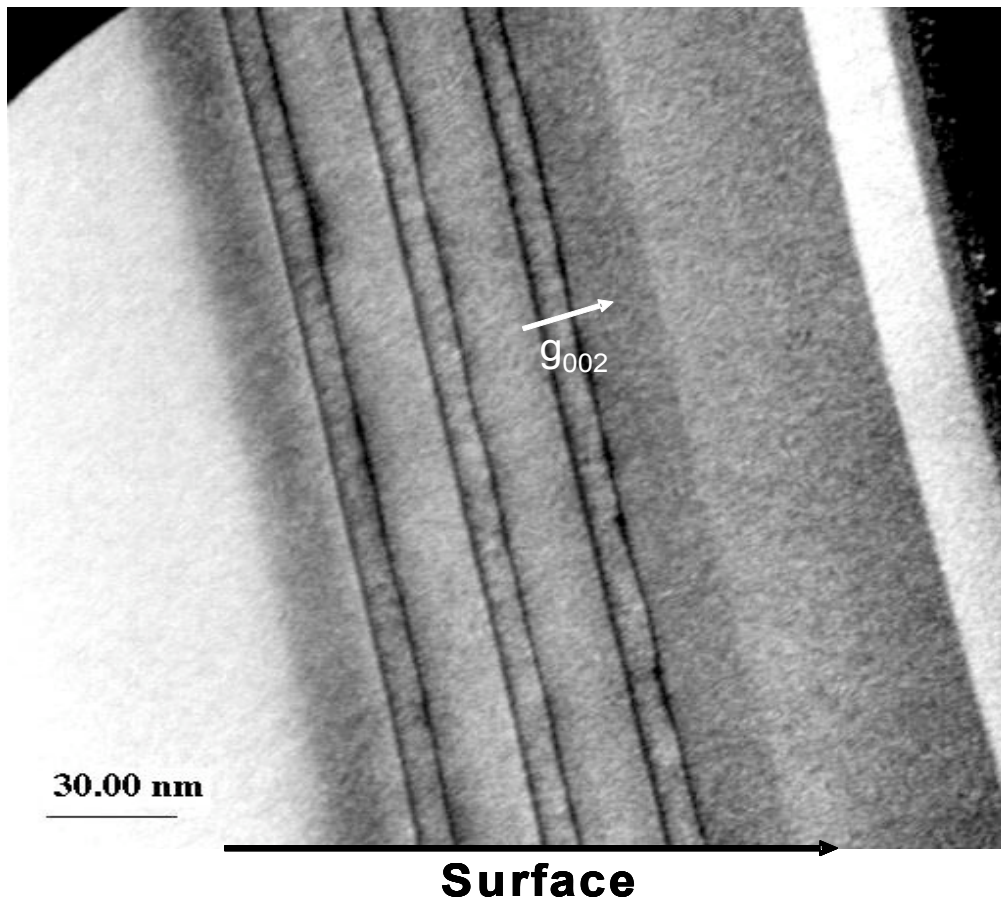


Figure 2.26: DF (002) image of triple quantum well GaInNAs sample.

The (002) DF analysis is extremely useful in investigating the compositional uniformity within the wells as well as the integrity of the well interfaces. As expected for a GaInNAs sample, the wells in Figure 2.26 display a high degree of non-uniformity. There is evidence of clustering within the wells (shows up as contrast variation) and the well interfaces are rough, which is evidence of three dimensional growth. As previously observed, the deterioration is most severe for the top well.

Figure 2.27 shows the DF (002) image for a triple quantum well GaInNAs(Sb) sample.

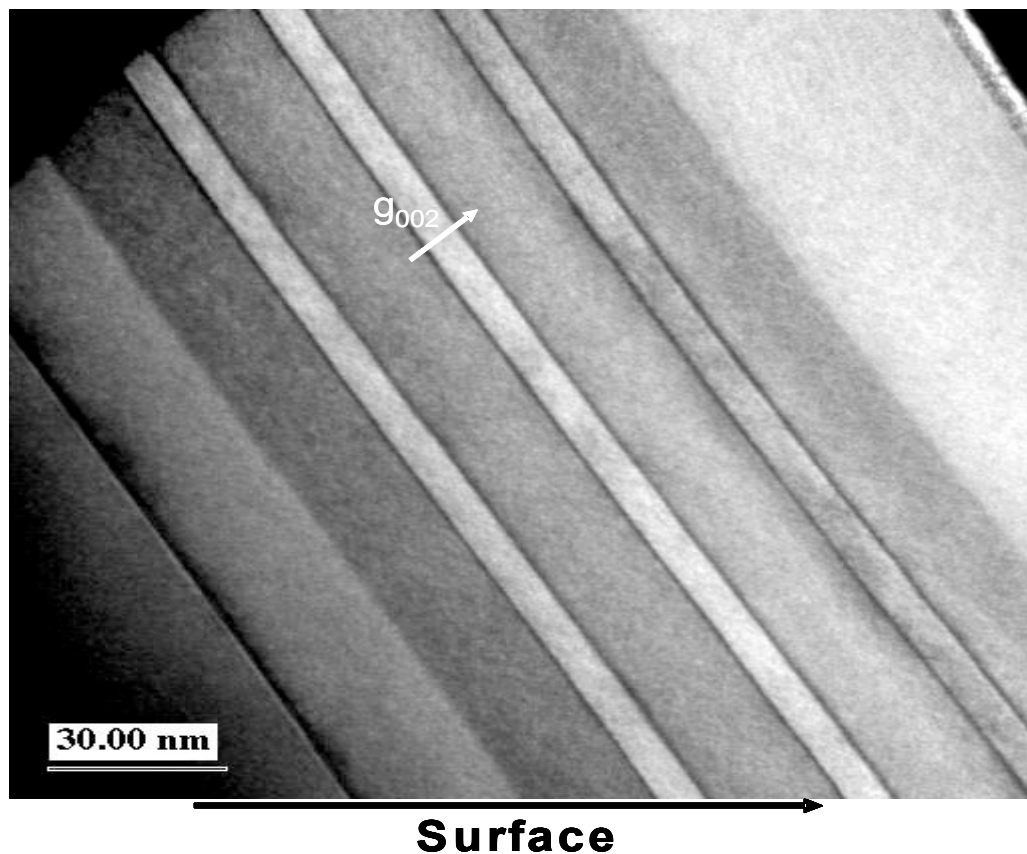


Figure 2.27: DF (002) image of triple quantum well GaInNAs(Sb) sample.

Figure 2.27 shows that antimony plays a big role in improving the compositional uniformity. Compared to the GaInNAs sample in Figure 2.26, the GaInNAs(Sb) sample in Figure 2.27 shows sharp and smooth well interfaces. There is very little variation of contrast within the wells and even the top well shows very good uniformity. The DF (002) images once again confirm the findings from the strain maps that antimony is responsible for the improved uniformity in the quantum well region.

Chapter 3: Effect of Growth Conditions on the Microstructure

This chapter will discuss three different effects of the growth conditions on the GaInNAs(Sb) alloy in the context of TEM. High Resolution and Dark-Field imaging results are presented to investigate the structural effects of 1) Growth temperature variation, 2) Anneal and 3) Deflection plates in front of the nitrogen plasma cell.

3.1 Growth Temperature Effects

As already discussed in the previous chapter, we suspect that there is some heating that occurs during the growth of subsequent quantum wells. This is due to the fact that the active region material has a smaller bandgap than the substrate and is able to absorb far more of the IR radiation from the heater. In order to investigate the effects of this heating on the microstructure, we prepared two sets of samples: one where the growth temperature was kept constant and one where the growth temperature was dropped by 5 °C per quantum well. The idea behind dropping the temperature was to try and compensate for the heating effect during the growth. The TEM investigation was done on triple quantum well GaInNAs(Sb) samples. Strain maps and DF (002) and (220) images were obtained for both sets of samples.

Figure 3.1 shows the strain map for the sample grown at constant growth temperature and Figure 3.2 shows the map for the sample where the temperature was dropped by 5 °C.

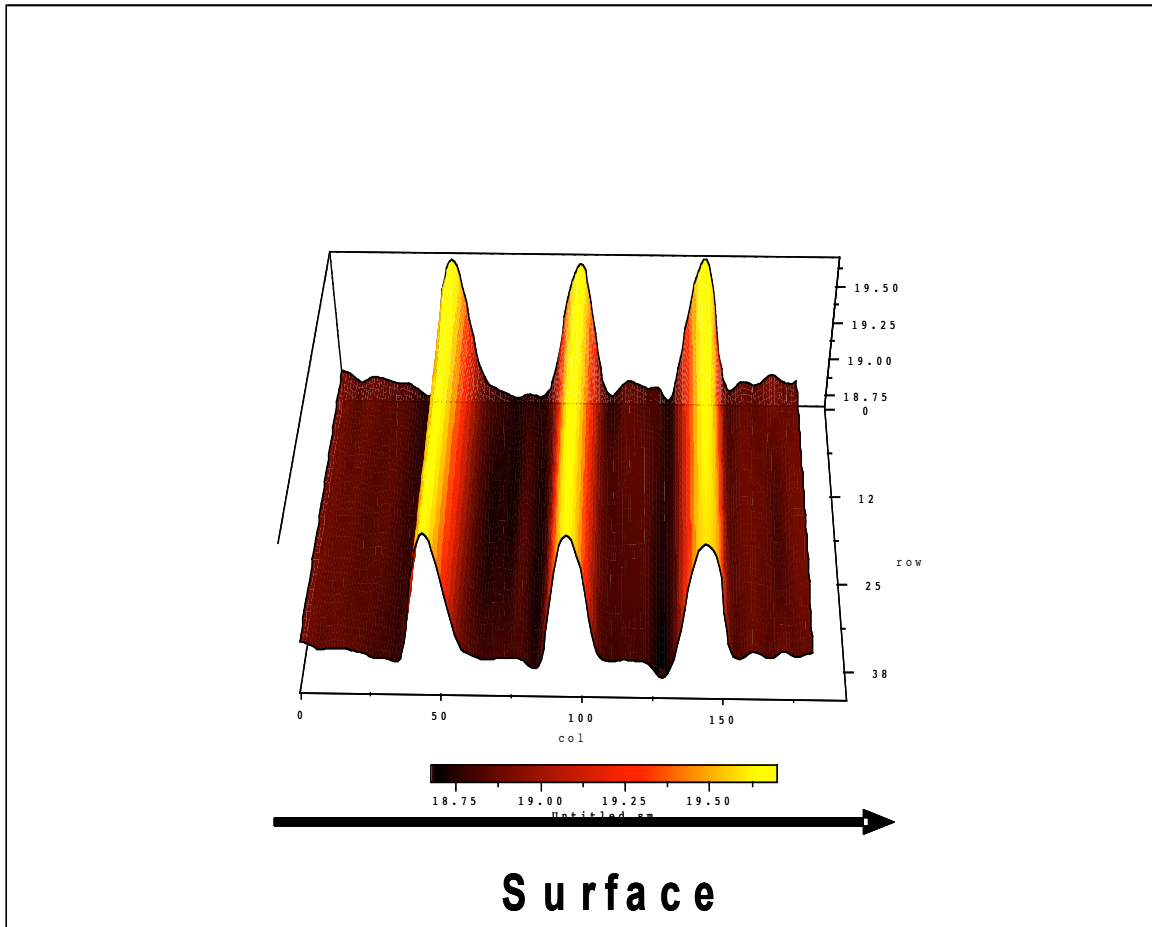


Figure 3.1: Strain map of triple quantum well GaInNAs(Sb) sample. The temperature was constant during growth.

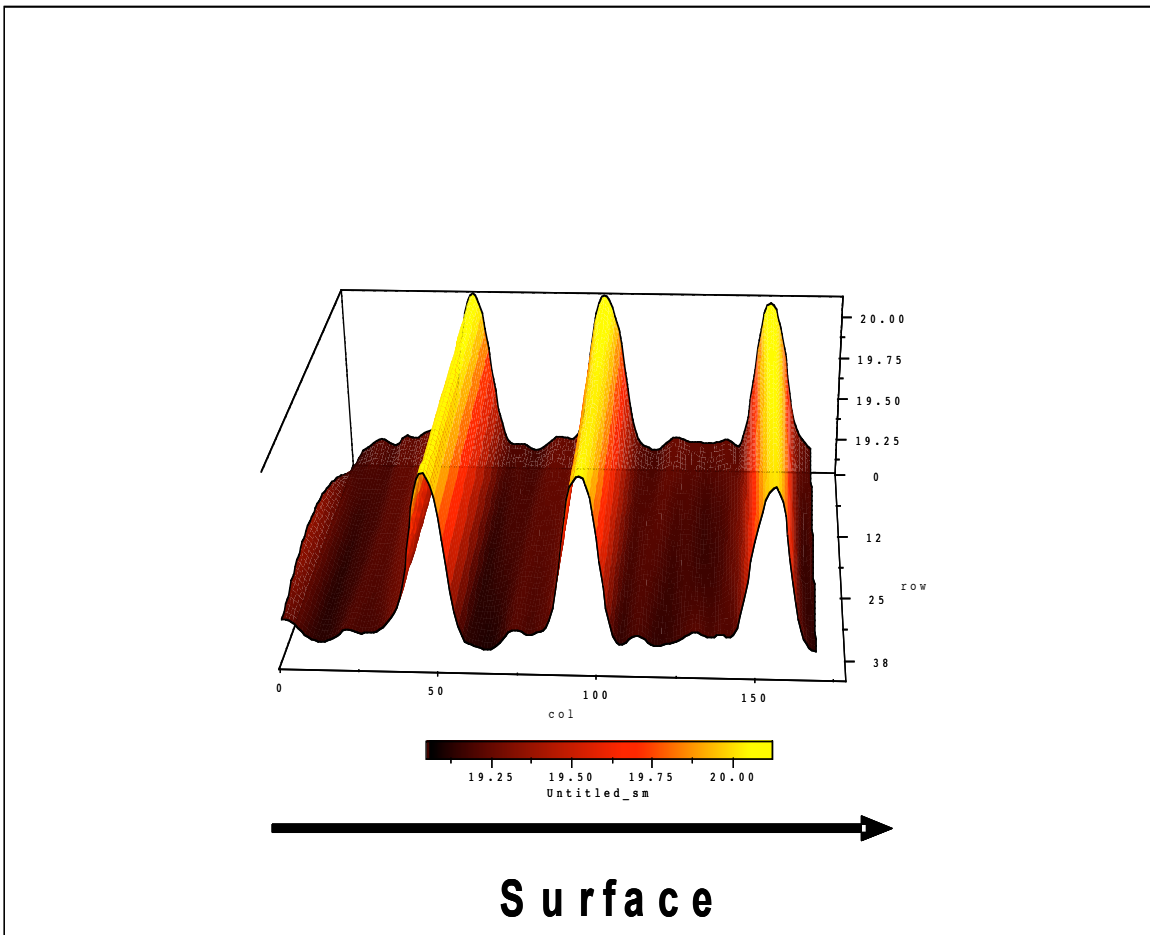


Figure 3.2: Strain map of triple quantum well GaInNAs(Sb) sample. The temperature was dropped 5 °C per quantum well.

From Figures 3.1 and 3.2, we see that the compositional profiles are very uniform as we can expect from growth in the presence of antimony. An interesting feature in Figure 3.1 (which is absent in Figure 3.2) are the tensile spikes that are observed in the barrier region just before the bottom well interfaces. The barriers consist of GaNAs with about 2.3% nitrogen. We refer to

these features as tensile spikes because they are in a direction opposite to the quantum well peaks and signify regions with smaller lattice constant. They result from higher nitrogen concentration at the bottom well interfaces. The origin of these spikes lies in the particular growth method used for these samples. The barriers do not contain any antimony and the antimony flux is turned on just before the growth of each well to act as a surfactant, and turned off before the next barrier is grown. Some studies in our group on the interaction between nitrogen and antimony have shown that the presence of antimony leads to an increased nitrogen incorporation [27]. This results in the tensile spikes that are observed before each successive well. An examination of Figure 3.2 shows that these spikes are not present in the sample where the growth temperature was dropped 5 °C per well. We are not clear as to the reason why this occurs, but we suspect that the drop in temperature changes the interaction mechanism between the antimony and the nitrogen. As a result, nitrogen does not incorporate in excess amount in the interface region. This is actually very good news for real device performance. The tensile spikes are areas of higher nitrogen concentration which effectively means a smaller bandgap as well. This smaller bandgap in the barrier decreases the confinement of the electrons in the quantum wells which affects adversely the temperature performance of the laser. It seems that a slight drop in the growth temperature during well growth can be beneficial in terms of eliminating the tensile spikes.

Figures 3.3 and 3.4 show the DF (002) images for the constant growth temperature sample and the 5 °C temperature drop sample respectively.

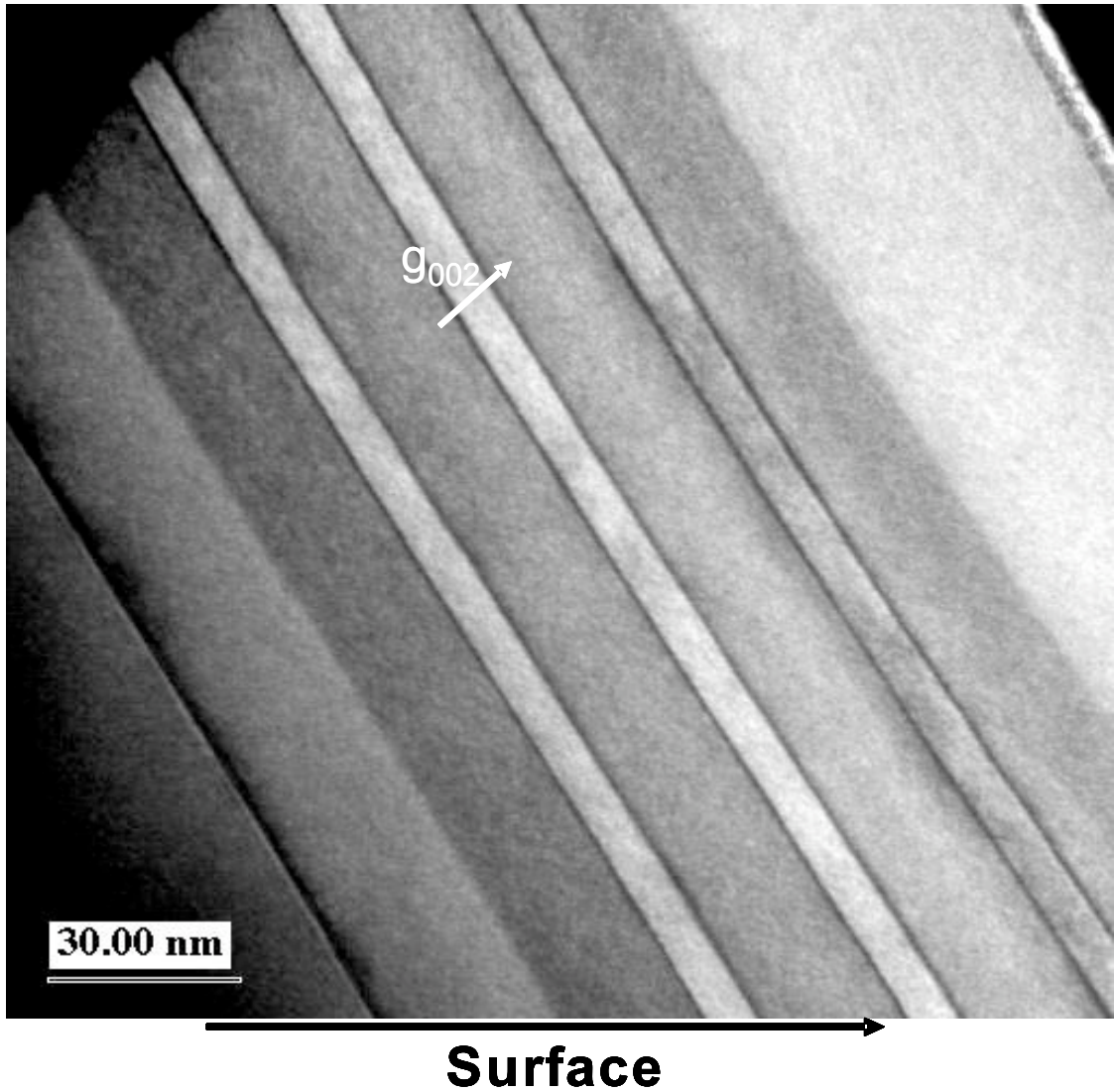


Figure 3.3: DF (002) image of triple quantum well GaInNAs(Sb) sample. The temperature was constant during growth.

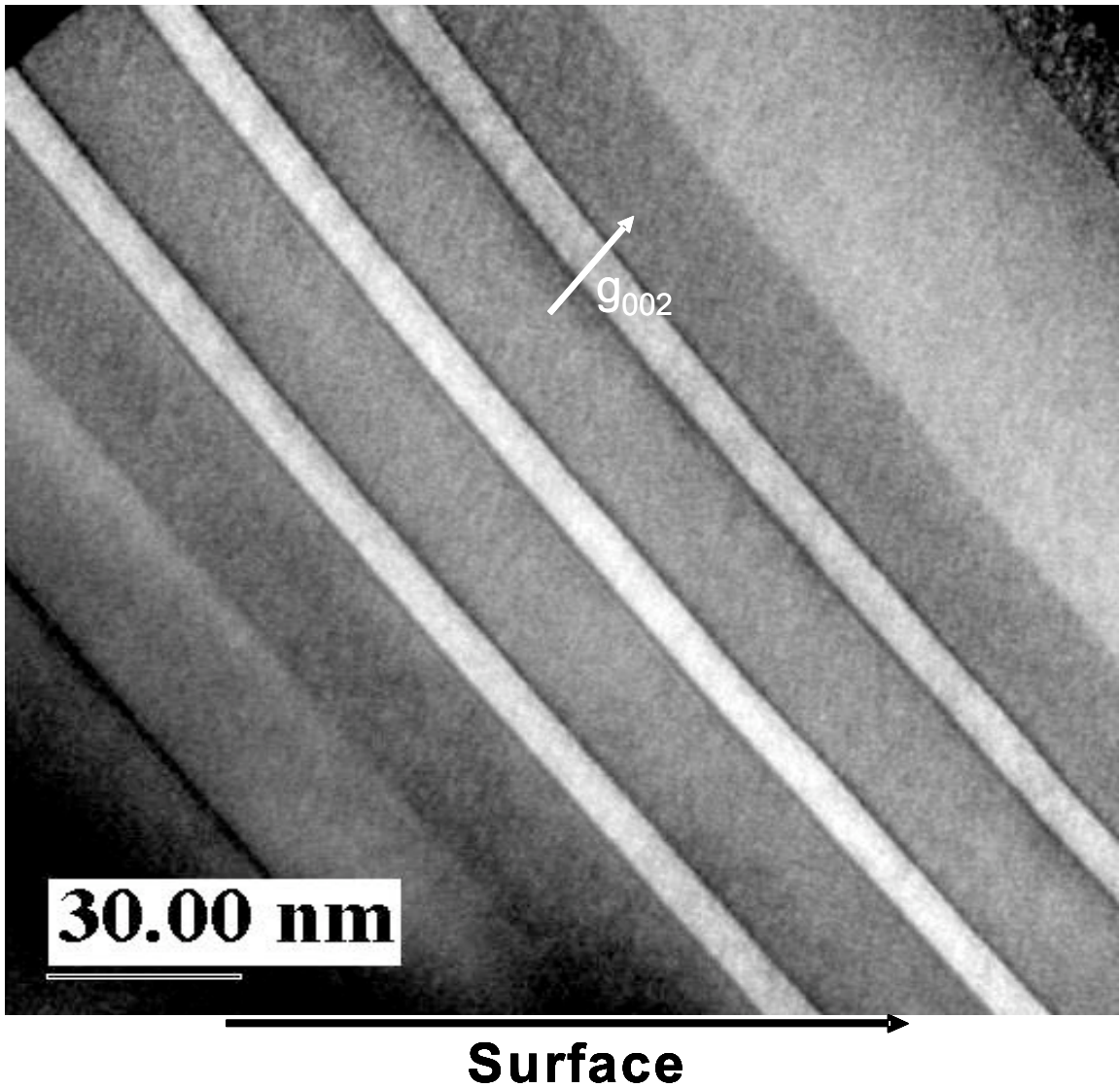


Figure 3.4: DF (002) image of triple quantum well GaInNAs(Sb) sample. The temperature was dropped 5 °C per quantum well.

Figure 3.4 shows that a slight drop in the temperature during growth produces an additional (although quite marginal) improvement in the uniformity and smoothness of the quantum well interfaces. This effect is better registered with DF images with the (220) reflection. The reciprocal vector for the (220) reflection is parallel to the quantum wells and is sensitive to compositional variations along the wells. Figures 3.5 and 3.6 show the DF (220) images for the two samples.

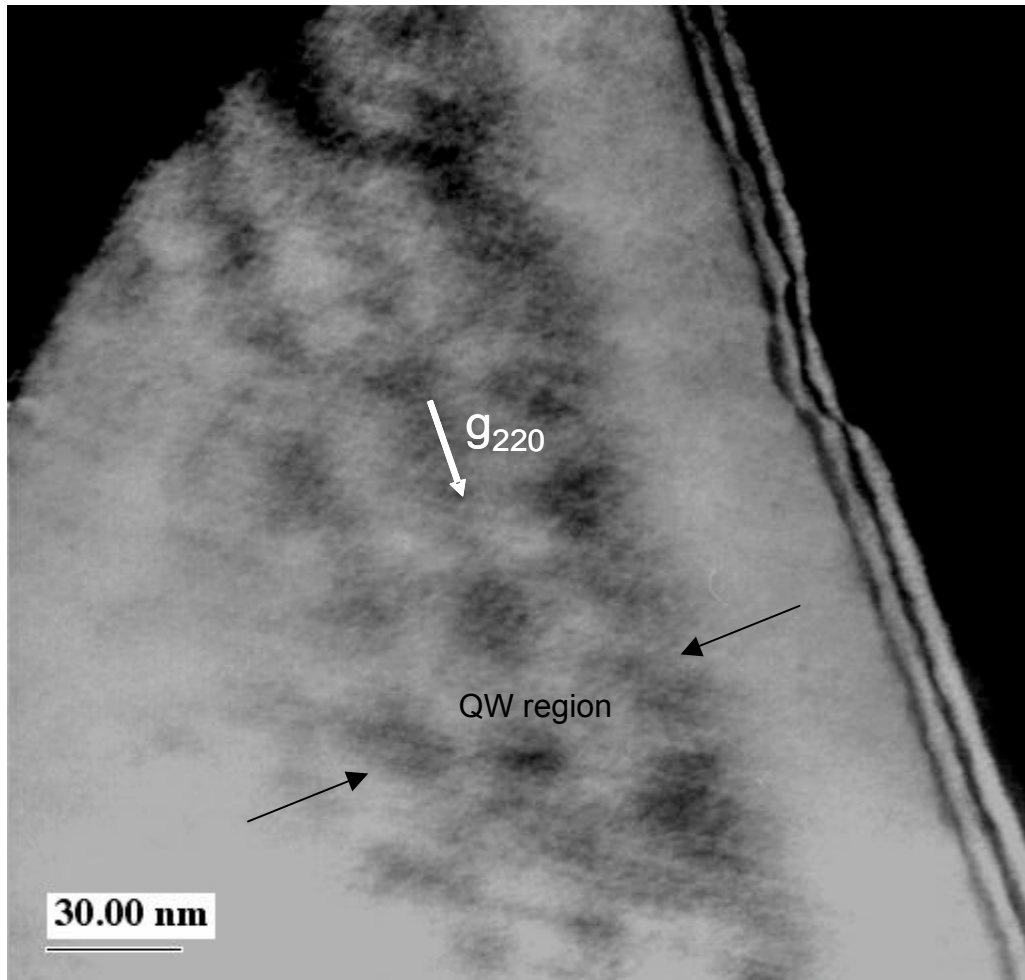


Figure 3.5: DF (220) image of triple quantum well GaInNAs(Sb) sample. The temperature was constant during growth.

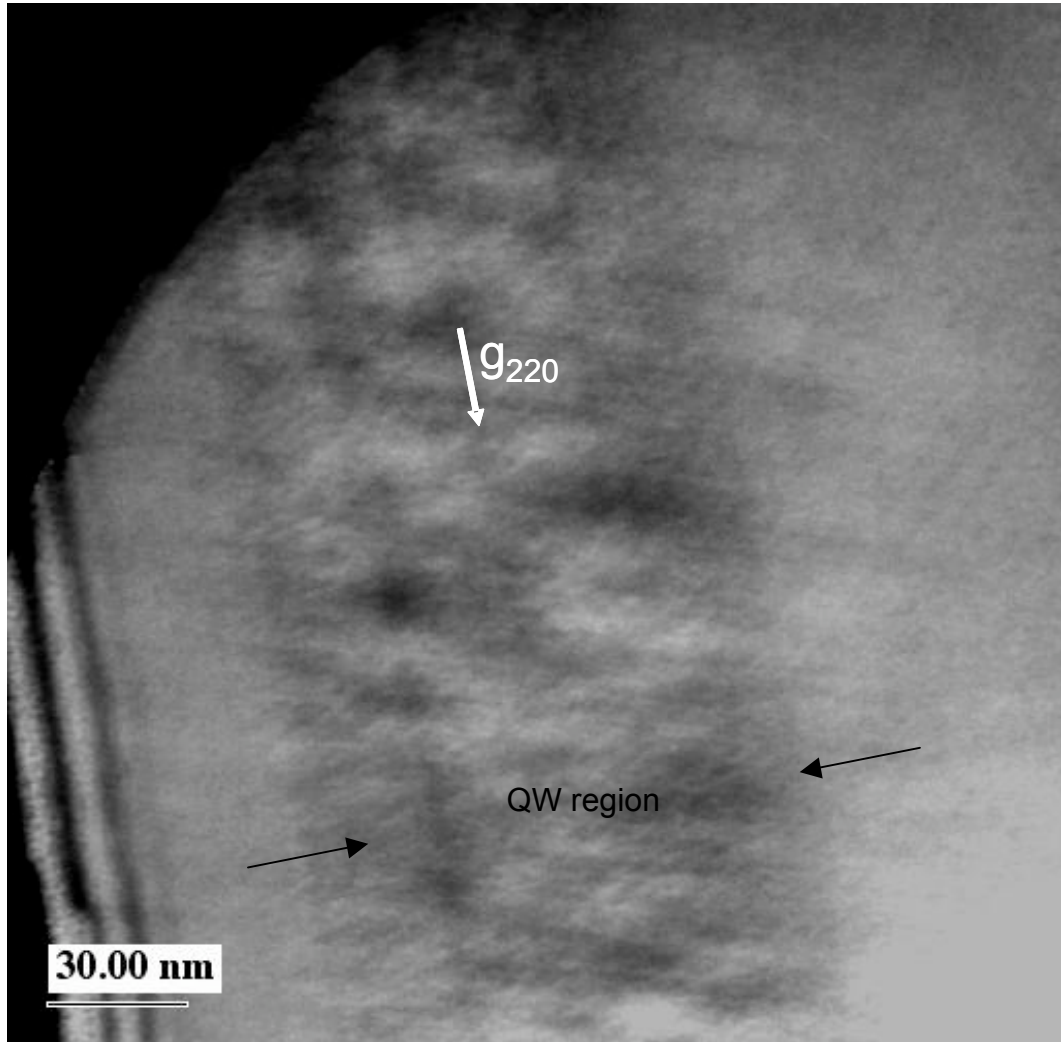


Figure 3.6: DF (220) image of triple quantum well GaInNAs(Sb) sample. The temperature was dropped 5 °C per quantum well.

Figure 3.5 shows more pronounced contrast variation along the quantum well region. This variation in the contrast is evidence of lateral compositional fluctuations. Figure 3.6 shows that the contrast variation is less severe and lends support to the notion that reducing the temperature during well growth can be beneficial in terms of improved compositional uniformity.

3.2 Anneal Effects

This section presents a brief discussion on the effects of annealing on the microstructure of GaInNAs(Sb) in the context of TEM. Due to the metastable growth of this alloy at low temperatures, a large number of imperfections are introduced in the crystal. This requires that GaInNAs(Sb) be annealed post growth in order to remove the defects and improve the luminescence efficiency. The typical annealing routine is Rapid Thermal Anneal (RTA) for short times (around one minute) and high temperatures (around 800 °C). This mainly serves to remove point defects (i.e. vacancies and interstitials) which act as non-radiative recombination centers and greatly reduce the luminescence efficiency. The TEM analysis was employed to investigate whether any other structural changes (beyond point defect elimination) occur during the annealing process. Figures 3.7 and 3.8 show the strain maps for triple quantum well GaInNAs(Sb) samples in the unannealed and annealed conditions respectively.

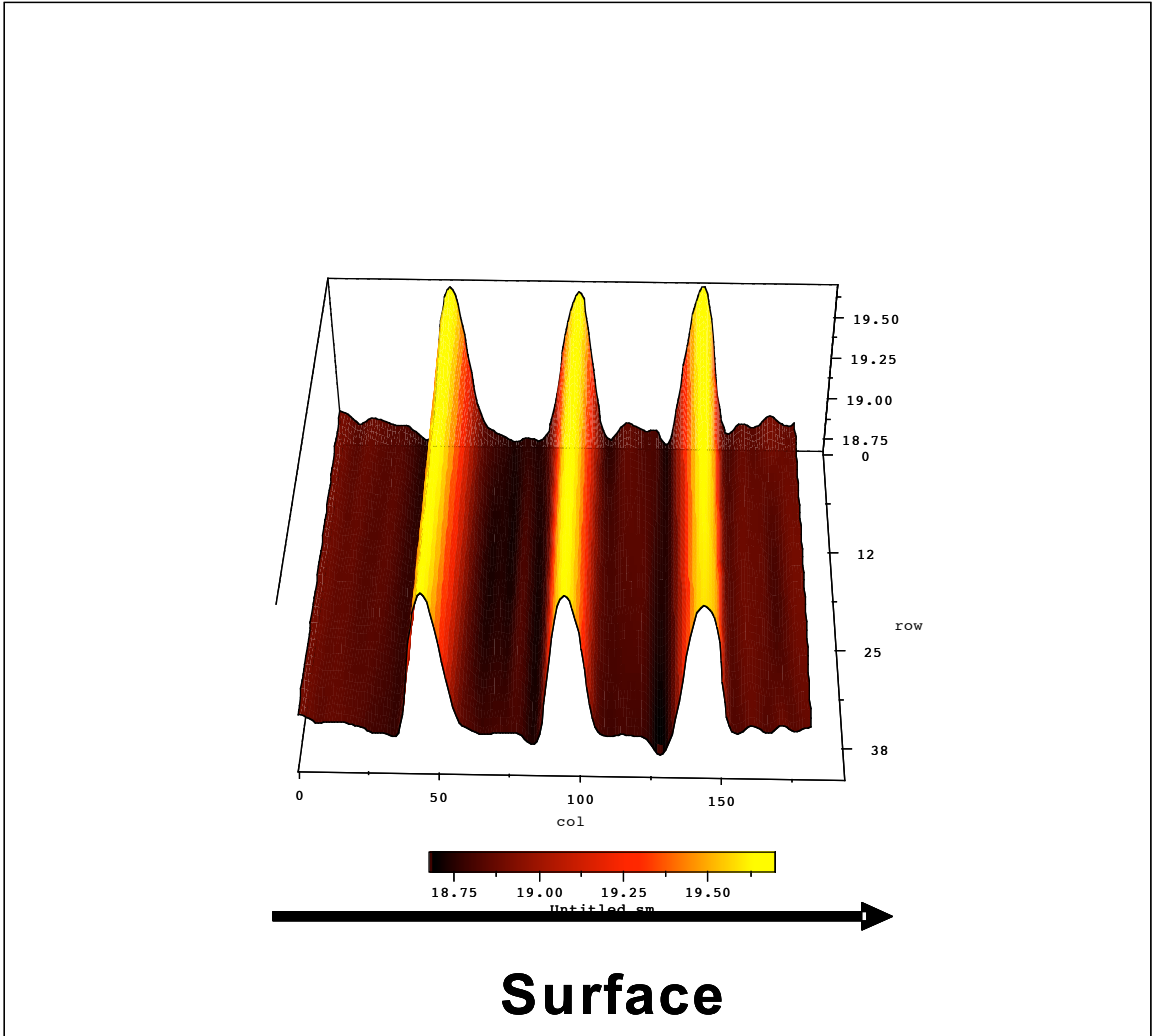


Figure 3.7: Strain map of unannealed triple quantum well GaInNAs(Sb) sample.

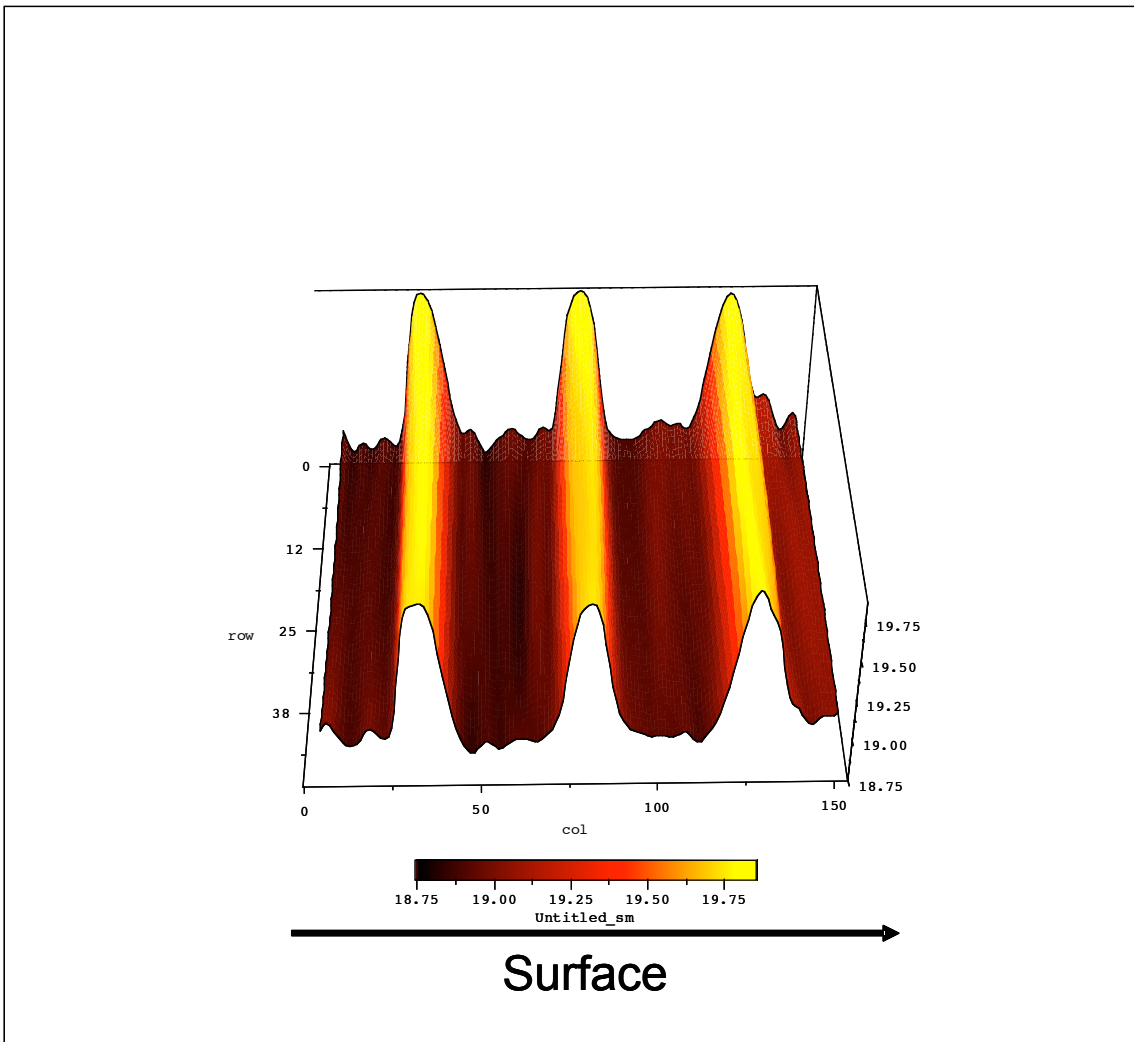


Figure 3.8: Strain map of annealed triple quantum well GaInNAs(Sb) sample.

It is evident from Figures 3.7 and 3.8 that annealing does not produce any discernable structural changes in the quantum wells. The profile uniformity is good for both samples and the sharp interfaces are preserved after the anneal process. This observation confirms our initial hypothesis that annealing does not

have a major effect on indium clustering in the wells. Rather, its importance lies in annealing out the point defects and improving the luminescence efficiency.

3.3 Deflection Plates Effects

This section discusses the “deflection plates” effect as a recent addition to our material growth practice, which led to a significant improvement in the optical quality of the material [35-37]. During MBE growth of GaInNAs(Sb), nitrogen is supplied with a radio-frequency (RF) plasma cell. In addition to atomic nitrogen (which is the desirable form and incorporates substitutionally), the plasma cell also generates a variety of charged nitrogen radicals. These are accelerated by the RF field and bombard the sample at high energies. Thus, they introduce defects into the crystal and impart energy onto the lattice which promotes indium surface migration and clustering. To prevent these charged radicals from reaching the surface of the sample, we installed two metal plates in front of the plasma cell which, when properly biased, can deflect the charged species. After installing the plates, we observed a significant improvement in the optical performance of the material. We used TEM to determine whether there is any correlation between structural changes in the material and the improved optical qualities as a result of the deflection plates.

Figure 3.9 shows the strain map for a single quantum well GaInNAs(Sb) sample grown without the deflection plates and Figure 3.10 shows the strain map for an identical sample but grown with the deflection plates under bias.

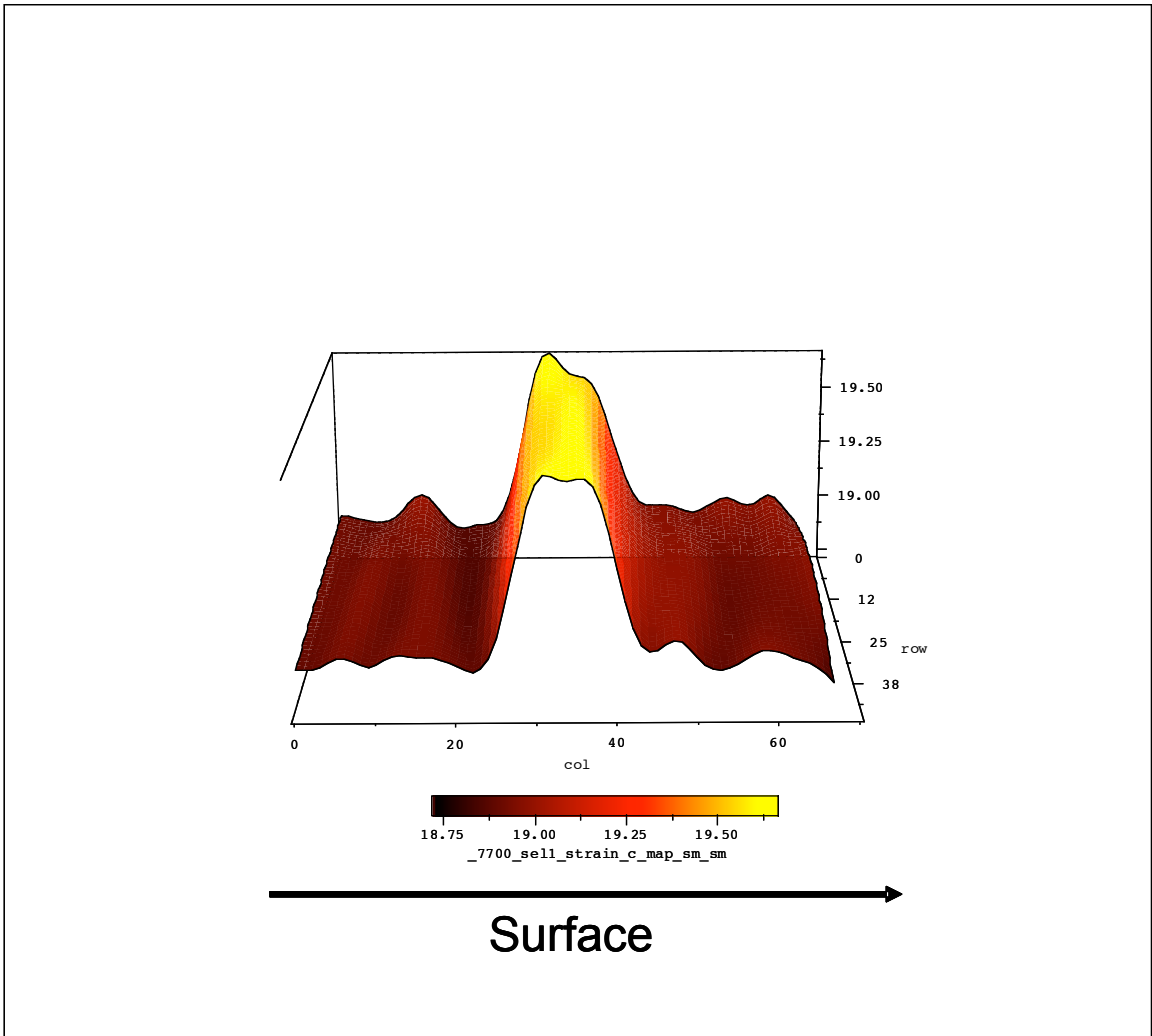


Figure 3.9: Strain map of a single quantum well GaInNAs(Sb) sample. No deflection plates.

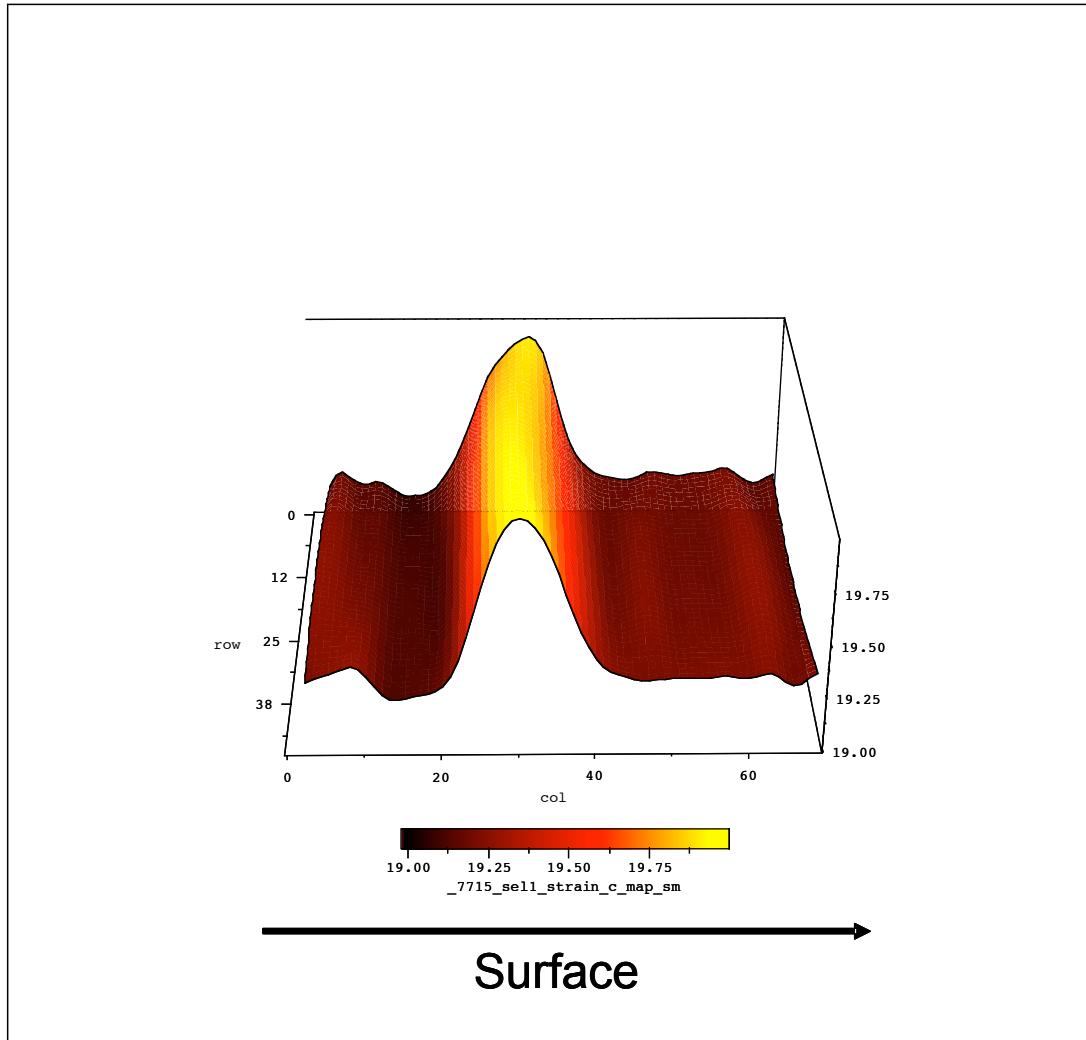


Figure 3.10: Strain map of a single quantum well GaInNAs(Sb) sample. With deflection plates.

The strain map in Figure 3.9 shows evidence of non-uniformities and clustering. Figure 3.10 shows a smoother profile and very little clustering. This is good evidence that the deflection plates are effective in preventing the high energy nitrogen radicals from reaching the surface and promoting indium migration and clustering.

The DF (002) images in Figure 3.11 (no deflection plates) and Figure 3.12 (with deflection plates) provide further evidence as to the benefit of using the deflection plates. Figure 3.11 shows that the top well interface is rough and shows evidence of clustering. Figure 3.12 shows that the well interfaces are smooth and there is very little clustering.

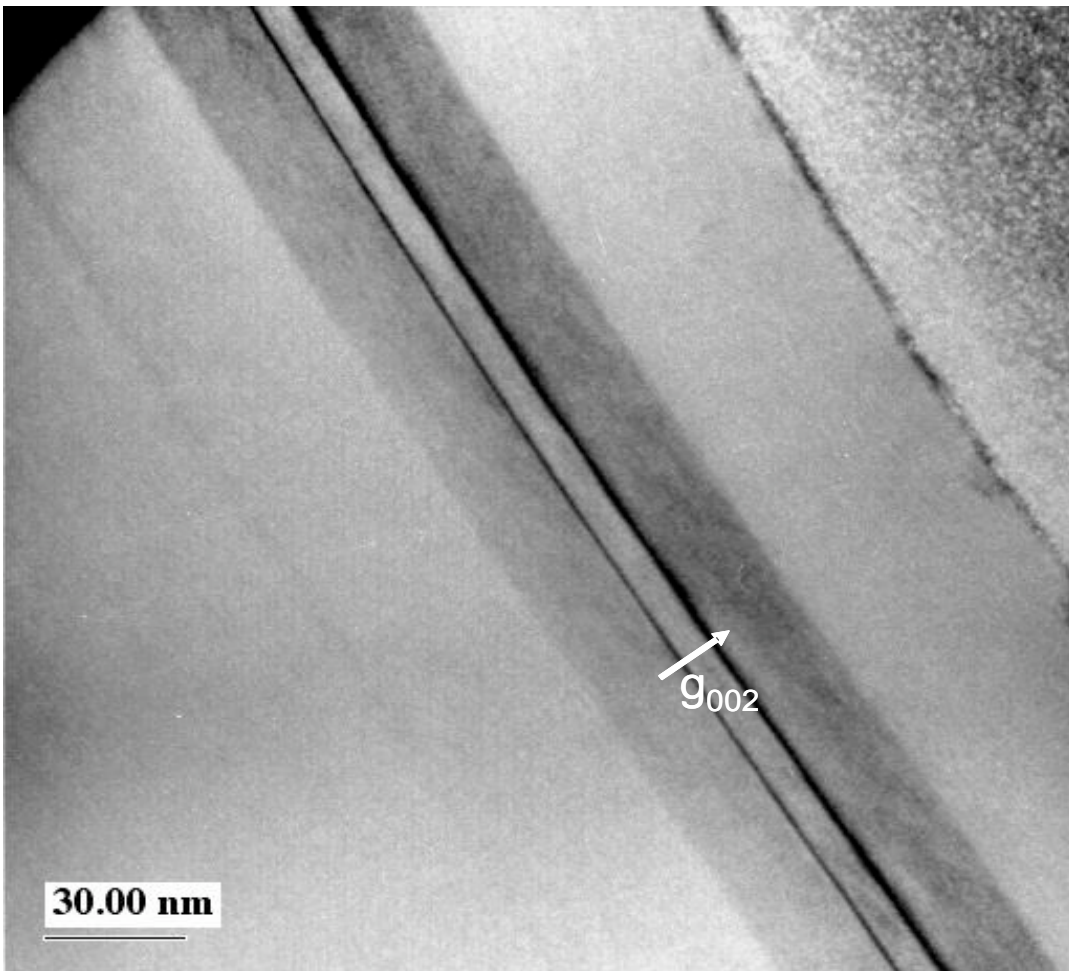


Figure 3.11: DF (002) image of a single quantum well GaInNAs(Sb) sample. No deflection plates.

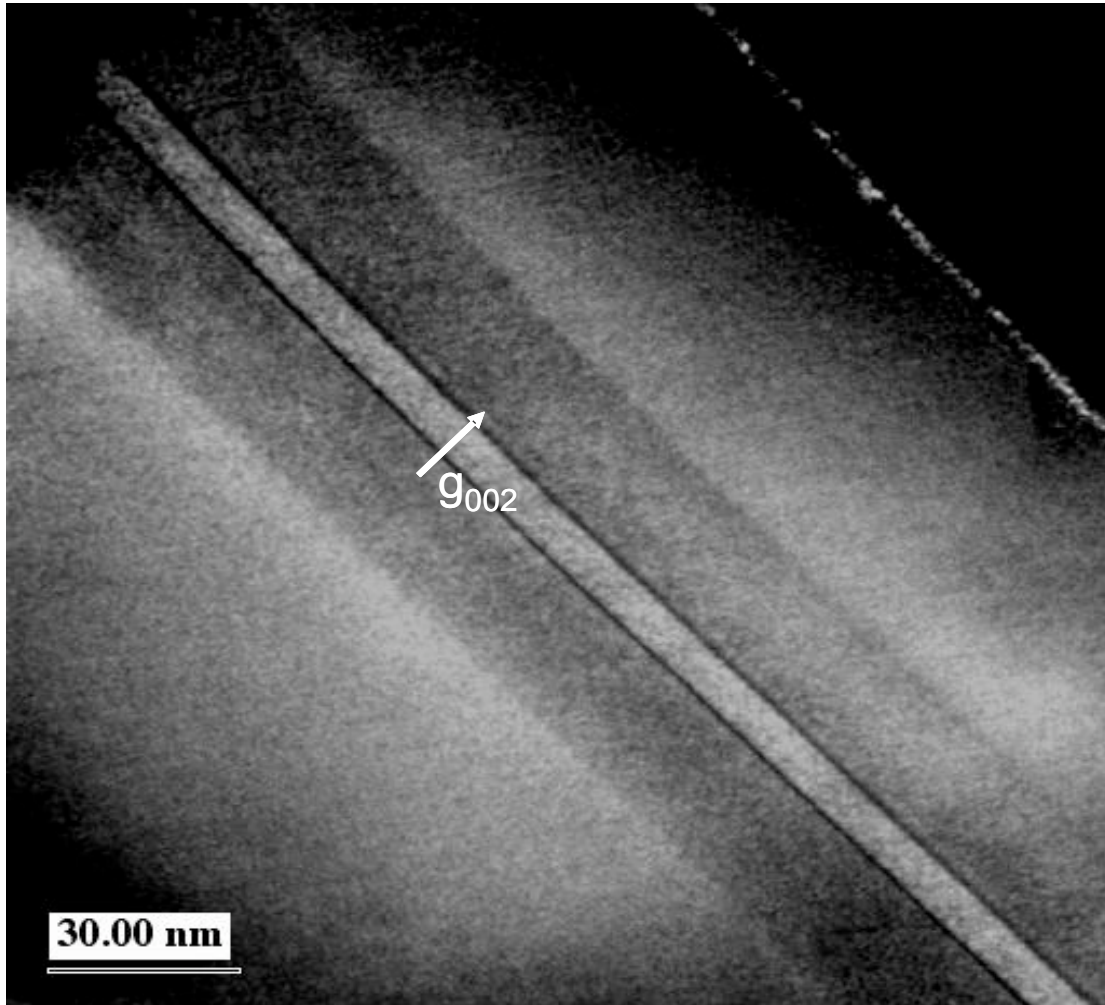


Figure 3.12: DF (002) image of a single quantum well GaInNAs(Sb) sample. With deflection plates.

The DF (220) images in Figures 3.13 (no deflection plates) and 3.14 (with deflection plates) are in excellent agreement with the strain maps and the DF (002) images. Figure 3.13 shows evidence of considerable lateral compositional fluctuation and clustering. Figure 3.14 shows a more uniform contrast along the well which signifies very little clustering. The DF (220) images are yet another

confirmation that growing with the deflection plates under bias improves the compositional uniformity.

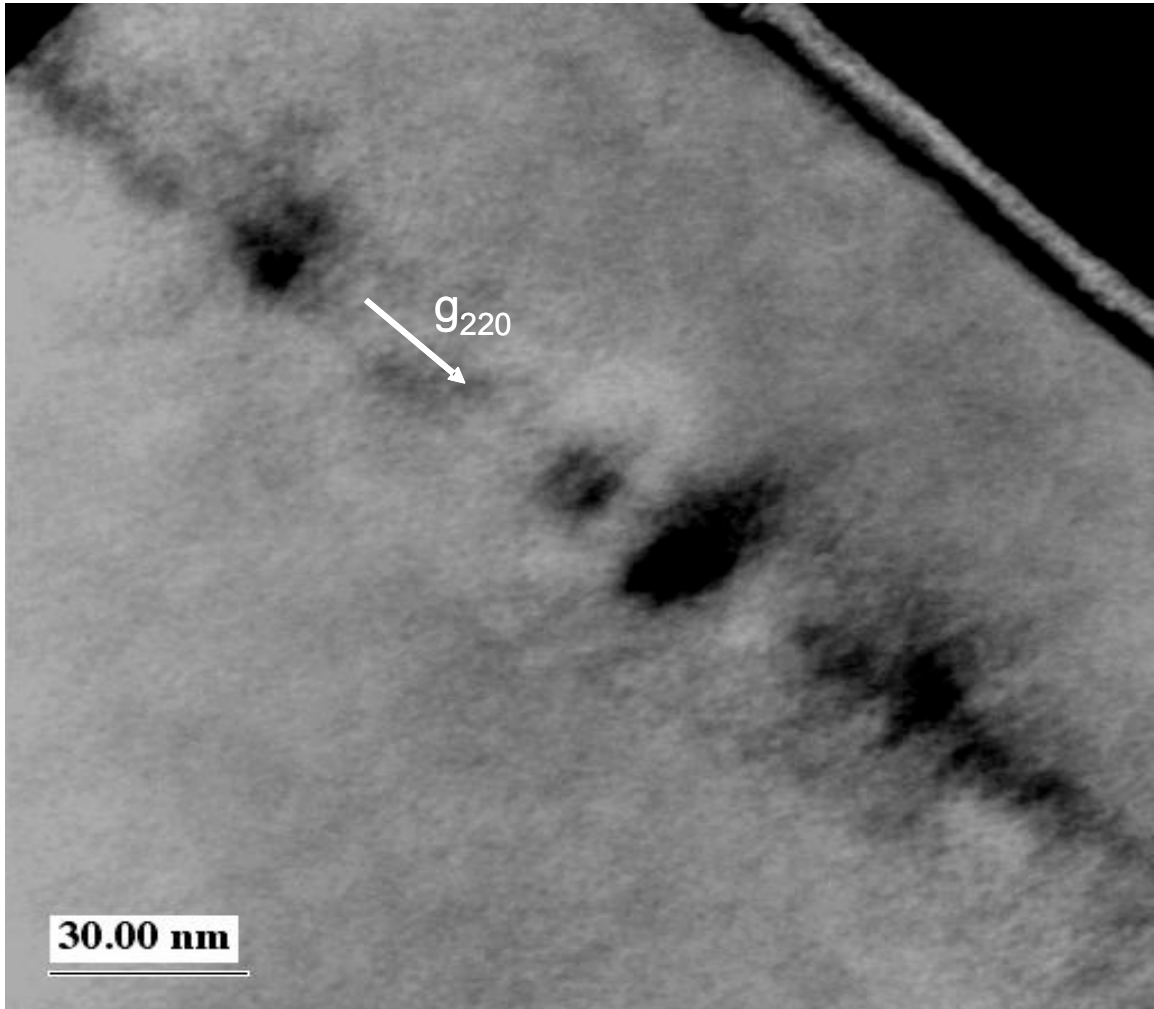


Figure 3.13: DF (220) image of a single quantum well GaInNAs(Sb) sample. No deflection plates.

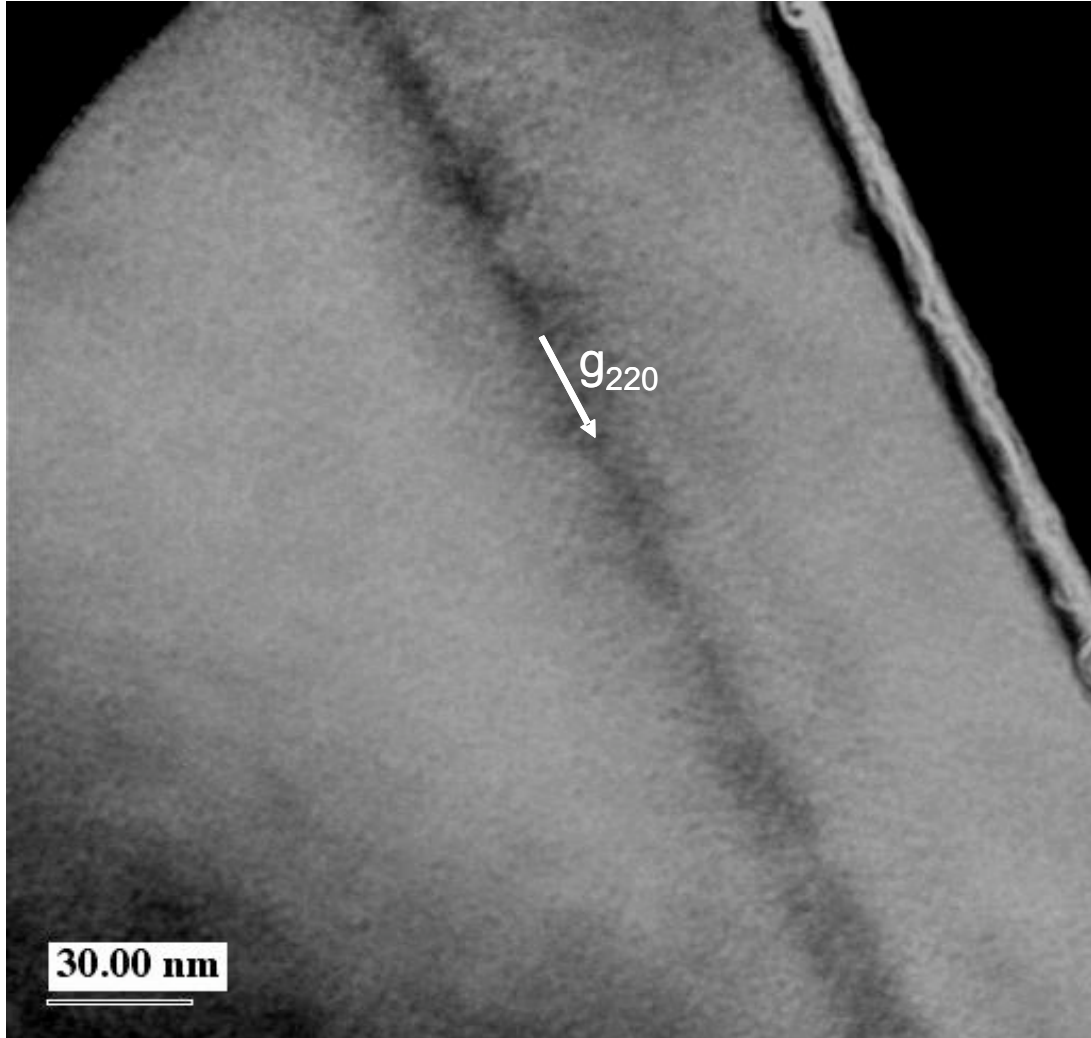


Figure 3.14: DF (220) image of a single quantum well GaInNAs(Sb) sample. With deflection plates.

Chapter 4: Conclusions and Future Work

4.1 Conclusions

In this work, we used Transmission Electron Microscopy to investigate the structural characteristics of GaInNAs and GaInNAs(Sb) quantum wells. Specifically, we investigated the compositional uniformity and well interface quality for these structures. We used four different TEM techniques to fully characterize GaInNAs and GaInNAs(Sb) samples: High Resolution (HRTEM) imaging, Energy-Filtered (EFTEM) imaging, Dark-Field (DF) imaging and Energy-Dispersive X-ray Spectroscopy (EDX). HRTEM analysis was conducted in a novel way: the HRTEM images were used to generate strain maps across the quantum well region of the samples in order to investigate the compositional fluctuations within the wells. Dark-Field images with the (002) and (220) reflections were obtained to investigate the quality of the well interfaces and verify the strain map findings. EFTEM images and EDX profiles were obtained to complement the strain map analysis. Photoluminescence and Cathodoluminescence measurements were used to correlate the material optical properties to the TEM structural analysis.

The TEM analysis established that:

- 1) Antimony dramatically improves the compositional uniformity and interface smoothness of GaInNAs quantum wells by acting as a reactive surfactant. Thus,

the addition of antimony during the growth is a crucial step towards better device performance and emission at longer wavelengths.

2) Slight temperature reduction during quantum well growth can be beneficial for device performance. It tends to further improve the uniformity in the top well and increase the carrier confinement by eliminating the tensile spikes in the barriers.

3) Use of voltage bias plates with the nitrogen plasma source further improves the uniformity of the material by deflecting high energy plasma radicals.

4) Annealing has little effect on the long-range segregation of indium but is important in annealing out the point defects which dramatically increases the luminescence efficiency of the material.

4.2 Future Work

There remain quite a few challenges down the road before GaInNAs(Sb) material can be grown with sufficient quality to compete with the currently used InP-based lasers. In the context of TEM, the strain map analysis can be used to further fine tune the indium/nitrogen ratio in the alloy in terms of growing the highest uniformity material with the best interface quality. This work briefly touched upon the structural changes in the material during the anneal process, but further TEM investigation should look at the effect of anneal parameters (temperature and time) on the structural quality of the wells. Finally, a Scanning Tunneling Microscopy (STM) study could be very useful in characterizing the nitrogen distribution.

Chapter 5: References

1. Source: Harris group viewgraphs.
2. J. S. Harris Jr., "GaInNAs long-wavelength lasers: progress and challenges," *Semicond. Sci. Technol.*, vol. 17, pp. 880-891, 2002.
3. J. Hecht, *Understanding Fiber Optics*. Upper Saddle River, NJ: Prentice Hall, 2002.
4. Source: James Harris viewgraph.
5. A. F. Phillips, S. J. Sweeney, A. R. Adams, and P. J. A. Thijs, "The temperature dependence of 1.3 and 1.55 μm compressively strained InGaAs(P) MQW semiconductor lasers," *IEEE J. Select. Topics Quantum Electron.*, vol. 5, pp. 301-352, 1999.
6. C. W. Coldren, M. C. Larson, S. G. Spruytte, and J. S. Harris Jr., "1200nm GaAs based vertical cavity lasers employing GaInNAs multiple quantum well active region," *Electron. Lett.*, vol. 36, no. 11, pp. 951-952, May 25, 2000.
7. S. Sato, Y. Osawa, T. Saitoh, and I. Fujimura, "Room-temperature pulsed operation of 1.3 μm GaInNAs/GaAs laser diode," *Electron. Lett.*, vol. 33, no. 16, pp. 1386-1387, July, 1997.
8. M. R. Gokhale, P. V. Studentkov, J. Wei, and S. R. Forrest, "Low threshold current, high efficiency 1.3 μm wavelength aluminum-free InGaAsN-based quantum-well lasers," *IEEE Photon. Tech. Lett.*, vol. 12, pp. 131-133, 2000.

9. M. Kondow, K. Uomi, A. Niwa, T. Kitantai, S. Watahiki, and Y. Yazawa, "GaInNAs: A Novel Material for Long-Wavelength-Range Laser Diodes with Excellent High-Temperature Performance," *Jpn. J. Appl. Phys.*, vol. 35, no. 2B, pp. 1273-1275, Feb., 1996.
10. W. Shan, W. Walukiewicz, J. W. Ager III, E. E. Haller, J. F. Geisz, D. J. Friedman, J. M. Olson, and S. R. Kurtz, "Band Anticrossing in GaInNAs Alloys," *Phys. Rev. Lett.*, vol. 82, no. 6, pp. 1221-1224, Feb. 9, 1999.
11. H. Soda, K. Iga, C. Kitahara, and Y. Suematsu, "GaInAsP/InP Surface Emitting Injection Laser," *Jpn. J. Appl. Phys.*, vol. 18, pp. 2329-2330, 1979.
12. Source: V. Gambin viewgraph
13. K. S. Giboney, L. R. Aronson, and B. E. Lemoff, "The ideal light source for datanets," *IEEE Spectrum*, vol. 35, pp. 43-53, 1998.
14. T. Kitatani, K. Nakahara, M. Kondow, K. Uomi, and T. Tanaka, "A 1.3- μm GaInNAs/GaAs Single-Quantum-Well Laser Diode with a High Characteristic Temperature over 200 K," *Jpn. J. Appl. Phys.*, vol. 39, pp. 86-87, 2000.
15. M. O. Fischer, M. Reinhardt, and A. Forchel, "Room-temperature operation of GaInAsN-GaAs laser diodes in the 1.5- μm range," *IEEE J. Select. Topics Quantum Electron.*, vol. 7, no. 2, pp. 149-151, Mar., 2001.
16. T. Kitatani, M. Kondow, T. Kikawa, Y. Yazawa, M. Okai, and K. Uomi, "Analysis of Band Offset in GaNAs/GaAs by X-Ray Photoelectron Spectroscopy," *Jpn. J. Appl. Phys.*, vol. 38, pp. 5003-5006, 1999.
17. P. Krispin, S. Spruytte, J. S. Harris, and K. Ploog, "Electrical depth profile of p-type GaAs/Ga(As,N) heterostructures determined by capacitance-voltage

- measurements," *J. Appl. Phys.*, vol. 88, pp. 4153, 2000.
18. M. Yano, H. Imai, and M. Takusagawa, "Analysis of threshold temperature characteristics for InGaAsP/InP double heterojunction lasers," *J. Appl. Phys.*, vol. 52, no. 5, pp. 3172-3175, May, 1981.
 19. N. K. Dutta and R. J. Nelson, "Temperature dependence of threshold of InGaAsP/InP double-heterostructure lasers and Auger recombination," *Appl. Phys. Lett.*, vol. 38, no. 6, pp. 407-409, Mar. 15, 1981.
 20. V. Lordi, H.B. Yuen, S.R. Bank, M.A. Wistey, and J.S. Harris Jr., "Nearest-Neighbor Distributions in Ga_{1-x}In_xNyAs_{1-y} and Ga_{1-x}In_xNyAs_{1-y-z}Sbz Thin Films Upon Annealing," *Phys. Rev. B*, Vol. 71, No. 12, pp. 125309-1-8, March 2005.
 21. J.S. Harris, *IEEE J. Sel. Top. Quantum Electron.* 6, 1145 (2000).
 22. A. Wagner, C. Ellmers, F. Höhnsdorf, J. Koch, C. Agert, S. Leu, M. Hofmann, W. Stolz and W.W. Rühle, *Appl. Phys. Lett.* 76, 271 (2000).
 23. A. Ramakrishnan, G. Steinle, D. Supper, C. Degen and G. Ebbinghaus, *Electron. Lett.* 38, 322 (2002).
 24. K. Volz, A.K. Schaper, A. Hasse, T. Weirich, F. Höhnsdorf, J. Koch and W. Stolz, *Mater. Res. Soc. Symp. Proc.* 619, 291 (2000).
 25. H. Shimizu, K. Kumada, S. Uchiyana, and A. Kasukawa, "High-performance CW 1.26 μ m GaInNAsSb-SQW ridge lasers," *IEEE J. Select. Topics Quantum Electron.*, vol. 7, no. 2, pp. 355-364, Mar., 2001.
 26. X. Yang, M. J. Jurkovic, J. B. Heroux, and W. I. Wang, "Molecular beam

- epitaxial growth of InGaAsN:Sb/GaAs quantum wells for long-wavelength semiconductor lasers," *Appl. Phys. Lett.*, vol. 75, no. 2, pp. 178-180, July 12, 1999.
27. S. Bank, W. Ha, V. Gambin, M. Wistey, H. Yuen, L. Goddard, S. Kim and J.S. Harris, *J. Crystal Growth* 251, 367 (2003).
28. S. Bank, M. Wistey, W. Ha, H. Yuen, L. Goddard, and J. S. Harris, *Electron. Lett.* 39, 1445 (2003).
29. K. Volz, V. Gambin, W. Ha, M.A. Wistey, H.B. Yuen, S.R. Bank, and J.S. Harris Jr., "The Role of Sb in the MBE growth of (GaIn)(NAsSb)," *J. Cryst. Growth*, Vol. 251, No. 1-4, pp. 360-6, April 2003.
30. M. O. Fischer, M. Reinhardt, and A. Forchel, "Room-temperature operation of GaInAsN-GaAs laser diodes in the 1.5- μ m range," *IEEE J. Select. Topics Quantum Electron.*, vol. 7, no. 2, pp. 149-151, Mar., 2001.
31. K. T. Faber and K. J. Malloy, *The mechanical properties of semiconductors, semiconductors and semimetals* Volume 37. Academic press, Inc., 1992, pp. 31.
32. Source: Danielle Chamberlin at Agilent.
33. M. Albrecht, V. Grillo, T. Remmele, H. Strunk, A. Egorov, Gh. Dumitras, H. Riechert, A. Kaschner, R. Heitz and A. Hoffmann, *Appl. Phys. Lett.* 81, 2719 (2002).
34. J.-M. Chauveau, A. Trampert, M.-A. Pinault, E. Tournie, K. Du and K. Ploog, *J. Crystal Growth* 251, 383 (2003).

35. S.R. Bank, M.A. Wistey, H.B. Yuen, V. Lordi, V.F. Gambin, and J.S. Harris Jr., "Effects of Antimony and Ion Damage on Carrier Localization in MBE-Grown GaInNAs," *J. Vac. Sci. Technol. B*, to be published.
36. M.A. Wistey, S.R. Bank, H.B. Yuen, L.L. Goddard, T. Gugov, and J.S. Harris Jr., "Protecting Wafer Surface During Plasma Ignition Using an Arsenic Cap," *J. Vac. Sci. Technol. B*, to be published.
37. M.A. Wistey, S.R. Bank, H.B. Yuen, and J.S. Harris Jr., "Low Voltages on Ion Deflection Plates Reduce Plasma Damage during GaInNAs Growth," *Appl. Phys. Lett.*, submitted.